ASIP 2005
USAF Aircraft Structural Integrity Program

POSTER SESSION PARTICIPANTS

AIRCRAFT WRECKAGE STRUCTURAL RE-CONSTRUCTION AND DAMAGE ANALYSIS
Jong-Sheng Chen, Aeronautical Systems Research Division/CSIST

THE CASE FOR USAGE MONITORING IN THE FLEET MANAGEMENT OF U.S. ARMY HELICOPTERS
David White, Avion Inc.

CASE STUDIES OF MITIGATION OF FOD, FRETTING FATIGUE, CORROSION FATIGUE AND SCC DAMAGE BY LOW PLASTICITY BURNISHING IN AIRCRAFT STRUCTURAL ALLOYS
Narayanan Jayaraman, Lambda Technologies

COMPOSITE PATCH DESIGN STUDY FOR EXTENSIVELY CORRODED WING PANELS LOADED IN COMPRESSION
Guilllaume Renaud, National Research Council Canada

CROSS-REFERENCE OF JSSG 2006 GUIDANCE WITH MIL-STD-1530C REQUIREMENTS
David Keller, USAF, Aeronautical Systems Center, Engineering Directorate

DEVELOPING GUIDELINES FOR BONDED REPAIR OF STRESS CORROSION CRACKING
Michael Brauss, Proto Manufacturing Limited

DISASSEMBLY AND INSPECTION OF C-5A 69-0004 SUBSECTIONS
James Suzel, S&K Technologies, Inc.

FATIGUE AND DAMAGE TOLERANCE ANALYSIS FOR CORRELATION BETWEEN LOADING TYPE AND SERVICE LIFE OF AGING AIRCRAFT
Seungbae Park, SUNY at Binghamton

IMPACT INDICATOR PAINTS FOR COMPOSITES
Bryan Koene, Luna Innovations Inc.

SPECTRUM COUPON TESTING OF THE FORCETEC^{R} RIVETLESS NUTPLATE FOR AN AGING MILITARY AIRCRAFT
Fraser McMaster, Southwest Research Institute

SURFACE AND SUBSURFACE EDDY CURRENT INSPECTIONS. DEMONSTRATION OF COMPUTER MODELING ADVANTAGES FOR TYPICAL PROCEDURES
Evgueni Todorov, Edison Welding Institute

X-RAY DIFFRACTION TECHNOLOGY: THE CURRENT STATE-OF-THE-ART FOR MEASURING RESIDUAL STRESS IN AEROSPACE STRUCTURES
Michael Brauss, Proto Manufacturing Limited

The Case for Usage Monitoring in the Fleet Management of U.S. Army Helicopters

Dr. Robert E. Vaughan
Aviation Engineering Directorate
Redstone Arsenal, AL

2005 USAF Aircraft Structural Integrity Program (ASIP) Conference
29 November - 01 December 2005
The Peabody Memphis ~ Memphis, Tennessee

David J. White
Avion, Inc.
Huntsville, AL

✓ *Army helicopters must remain affordable, available and safe while flying escalated operational tempos in increasingly harsh environments.*

✓ *Knowledge of actual operational usage provides the opportunity to refine scheduled parts replacement intervals and predict unscheduled replacements.*

▪ Force Mod A/C are at Mid Life.

Aircraft	Entered Service	Design Age
CH-47	1961	44+ years
UH-60	1978	27+ years
AH-64	1984	21+ years

▪ Will remain in service beyond 2030.

▪ Parts fall far short of design expectations.

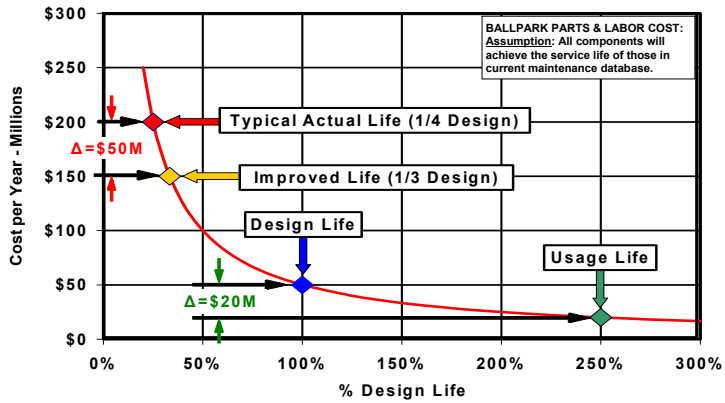

✓ *Monitor flight regime usage in operational environments and compare with design assumptions.*

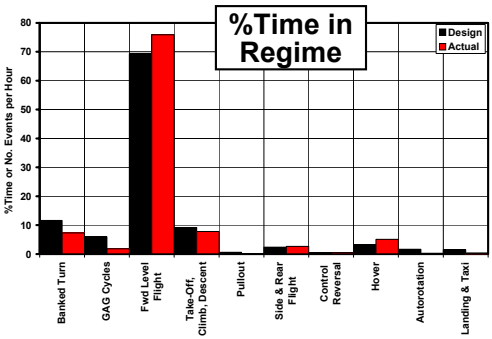

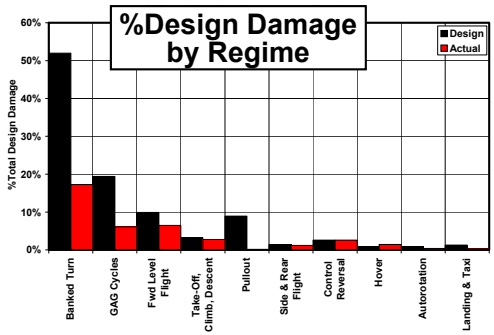

Operational Environment:

- ✓ Hot
- ✓ Temperate
- ✓ Cold
- ✓ Elevation
- ✓ Desert
- ✓ Tropics
- ✓ Maritime
- ✓ etc

✓ *Correlate flight regime usage in operational environments with actual parts replacements.*

▪ Usage/environment drive replacements.

✓ *Use regime recognition to determine usage.*
✓ *Develop algorithms that associate usage and environment with parts replacements.*
✓ *Monitor usage of each helicopter.*
✓ *Make informed decisions:*
- ▪ *Replace part?*
- ▪ *Modify usage?*

✓ *Predict impending parts replacements to improve:*
- ▪ *Safety*
- ▪ *Reliability*
- ▪ *Downtime*
- ▪ *Cost*

CASE STUDIES OF MITIGATION OF FOD, FRETTING FATIGUE, CORROSION FATIGUE AND SCC DAMAGE BY LOW PLASTICITY BURNISHING IN AIRCRAFT STRUCTURAL ALLOYS

N. Jayaraman (njayaraman@lambdatechs.com), Director of Materials Research
Paul S. Prevéy (pprevey@lambdatechs.com), President, Director of Research
Lambda Research, 5521, Fair Lane, Cincinnati, OH 45227 – 3401

ABSTRACT

Surface enhancement technologies such as shot peening (SP), laser shock peening (LSP) and low plasticity burnishing (LPB) can provide mitigation of foreign object damage (FOD), fretting fatigue, corrosion fatigue, and stress corrosion cracking (SCC) damage. However, to be effective, the compressive residual stresses must be retained in service for successful integration into aircraft structural design, and the process must be affordable and compatible with the manufacturing environment. LPB provides high magnitude deep thermally and mechanically stable compression, and is performed on CNC machine tools. LPB provides a means to extend the lives of both new and legacy aircraft structural components. Improving fatigue performance by introducing deep stable layers of compressive residual stress avoids the generally prohibitive cost of modifying either material or design.

The LPB process combined with an overview of current research programs is presented. Fatigue performance and residual stress data developed to date for several case studies conducted to apply LPB to a variety of aircraft components include:

- Improved fretting fatigue and corrosion fatigue performance with LPB in 4340 high strength steel
- LPB treatment to mitigate FOD, corrosion fatigue and SCC in 300M HSLA landing gear steel
- Corrosion pitting and corrosion fatigue mitigation with LPB in AA7075-T6
- Improved fatigue and corrosion fatigue performance of friction stir welded joints of AA2219-T8751

Where appropriate, the performance of LPB is compared to conventional shot peening.

INTRODUCTION

FOD, fretting, active corrosion fatigue, corrosion pitting, and SCC are generally recognized as degradation processes that affect aircraft structural components. These damage processes are usually divided into three stages, initiation, propagation, and failure. Damage is normally localized and limited to specific areas, while a major part of the structure remains unaffected. It is known that tensile stress above a threshold is necessary for damage propagation leading to failure. For example, a threshold stress intensity factor (SIF), ΔK_{th}, and a threshold SCC stress are commonly used in structural design. Similar thresholds exist for other damage processes such as fretting fatigue. Therefore, introducing residual compression of sufficient magnitude and depth in the damage-prone region will lead to a local net stress that is below the threshold, and hence achieve mitigation of the damage.

The classical approach to improve resistance to damage initiation and propagation is through alloy development and/or modification of microstructure through heat treatment. Protective coatings are also used to delay the onset of fretting and corrosion damage. Alloy development

programs are time consuming and can be very expensive, while application of protective coatings could have serious environmental impact.

Introduction of residual compressive stresses in metallic components has long been recognized[1,2,3,4] to lead to enhanced fatigue strength. Many engineering components have been shot-peened or cold worked with fatigue strength enhancement as the primary objective or by-product of a surface hardening treatment such as carburizing/nitriding, physical vapor deposition, etc. Over the last decade, treatments such as LPB[5], LSP[6], and ultrasonic peening[7] have emerged. In all surface treatment processes, optimal benefits are obtained when deep compression is achieved with minimal cold work of the surface. All of these surface treatment methods have been shown to improve the life and performance of fatigue prone engineering components to different degrees.

Low Plasticity Burnishing

LPB has been demonstrated to provide a deep surface layer of high magnitude compression in various aluminum, titanium, and nickel based alloys and steels with minimal cold work.[8] The deep compressive residual stress state on the surface of these materials mitigates fatigue damage including FOD[9,10,11] fretting,[12,13] and corrosion.[14,15,16,17] The LPB process can be performed on conventional CNC machine tools at costs and speeds comparable to conventional machining operations such as surface milling.

The LPB process has been described in detail previously,[19] and is characterized by a single pass of a smooth free rolling ball under a normal force sufficient to plastically deform the surface of the material. The ball is supported by a constant volume flow of fluid in a spherical hydrostatic bearing as shown in Figure 1, and can be held in any CNC machine or robotic positioning apparatus. The patented constant volume support prevents the ball from contacting the bearing surface. The ball is in solid contact only with the surface to be burnished and is free to roll on the surface of the work piece.

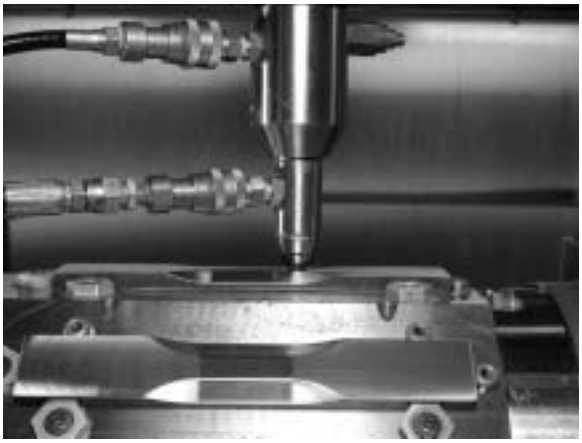

Figure 1 – LPB processing of fatigue samples with at single point contact LPB tool in a 4-axis CNC mill.

Using CNC positioning, the tool path is controlled during the LPB process so that the surface is covered with a series of passes at a separation maintained to achieve maximum compression with minimum cold working. The tool may be moved in any direction along the surface of a complex work piece, as in a typical multi-axis CNC machining operation. The LPB processing of fatigue specimens used in this investigation is also depicted in Figure 1.

EXPERIMENTAL TECHNIQUE

X-ray Diffraction Surface Characterization

Residual stresses were measured by standard x-ray diffraction method ($Sin^2\psi$). Appropriate corrections were applied to the measured residual stresses to account for redistribution of stresses from layer removal. Diffraction peak broadening, measured in conjunction with the residual stress, allows the amount of plastic deformation developed by surface enhancement methods to be accurately assessed. The method of quantifying the degree of cold working of metals, by relating the x-ray diffraction peak broadening to the equivalent true plastic strain, has been described previously.[20] The distribution of cold work as a function of depth into the deformed surface can be expressed in terms of the equivalent true plastic strain. If the degree of cold work is taken to be the equivalent amount of true plastic strain, the degree of cold work is then cumulative and is independent of the mode of deformation. Thus, the subsurface yield strength distribution can then be estimated from true stress-strain curves.[21] The macroscopic residual stress, of primary interest in design and life prediction, is determined in the conventional manner from the shift in the diffraction peak position.[22,23,24]

Test Methods

The HCF testing mode selected to provide maximum sensitivity to the surface condition was four-point bending.[25] Fatigue testing was conducted on thick section specimens at room temperature under constant sinusoidal load amplitude at 30 Hz, R=0.1 using Sontag SF-1U fatigue testing machines. Fatigue data were developed as S/N curves of nominally eight samples each. HCF samples were all typically finish machined by low stress grinding. In order to minimize the surface residual stresses from machining, the specimens were subsequently stress relieve annealed or electropolished. In all cases, the surface residual stresses of the as-machined specimens were documented. S/N curves were prepared for various combinations of surface conditions, fretting damage, corrosion damage, corrosive environment, and/or FOD.

Salt fog corrosion samples were exposed at 35° C per ASTM B117 for a period of 100 hours. Following exposure to the salt fog, residual salt was removed by soaking and then rinsing the samples in tap water, followed with a distilled water rinse. Patches of corrosion product evident on the surface of the samples were examined by x-ray diffraction. The corrosion product was not removed prior to fatigue testing.

Active corrosion fatigue tests were conducted with the sample gage section wrapped in a chemical-free laboratory tissue saturated with 3.5-wt% NaCl solution (pH adjusted) and sealed with polyethylene film and vinyl to avoid evaporation. The saturated tissue served as a wick to maintain the salt solution in contact with the sample surface.

Fretting damage was produced in thick section specimens by pressing a cylindrical pad into the active gage section of the fatigue specimen during cyclic loading. The clamping fixture was instrumented with strain gages and calibrated to monitor the normal force during testing.

SCC testing was completed on C-ring specimens with the gage section machined similar to the thick section specimen. The C-ring specimens were loaded with a diametral bolt, and load was monitored with instrumented washers. SCC testing was completed in an alternate immersion set up with 3.5% NaCl neutral salt solution with the specimens immersed for 10 minutes and out of the solution for 50 minutes for a total of 1 hour per cycle. Tests were terminated upon failure or after 1500 hours of test time.

FOD was simulated by introducing a v-shaped surface notch on the gage section by electrical discharge machining (EDM).

RESULTS AND DISCUSSION

High Strength Structural Steels

Ultrahigh strength steels such as 4340 and 300M are widely used in applications where a combination of high strength and fracture toughness is needed. Most of these ultrahigh strength steels have been known to be prone to SCC and corrosion fatigue.

4340 Steel

The residual stress profiles in LPB treated 4340 steel are shown in Figure 2. Measurements made both parallel and perpendicular to the treatment directions are presented. In both orientations, compression to depths greater than 0.050 in. (1.25 mm) is observed. The corresponding % cold work is well below 3%, even at the surface of the specimens.

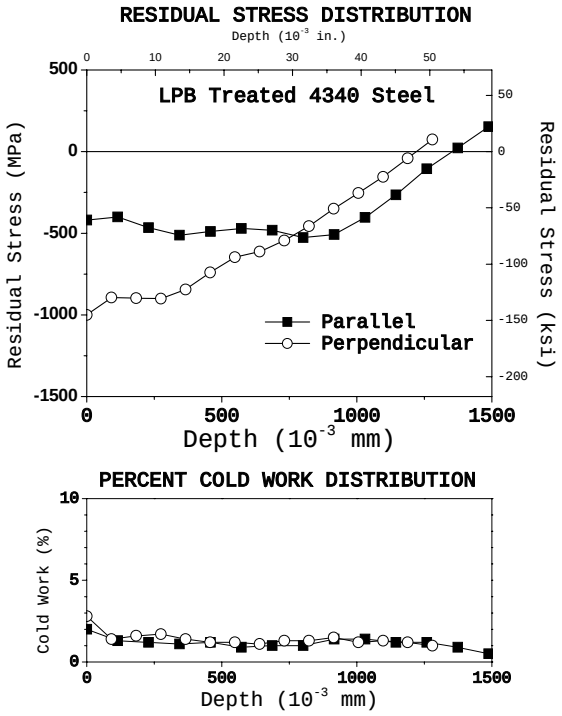

Figure 2 - Residual stress and % cold work distribution in LPB treated 4340 Steel

Figures 3 and 4 show the fatigue performance in the as-machined and LPB treated conditions before and after salt-fog exposure to 100 and 500 hours. It is evident from these figures that prior corrosion damage leads to a substantial debit in fatigue performance. LPB treatment results indicate significantly better fatigue performance than the as-machined condition. Also, both the S-N data and the bar chart indicate effective mitigation of damage from salt-fog exposure in LPB treated material.

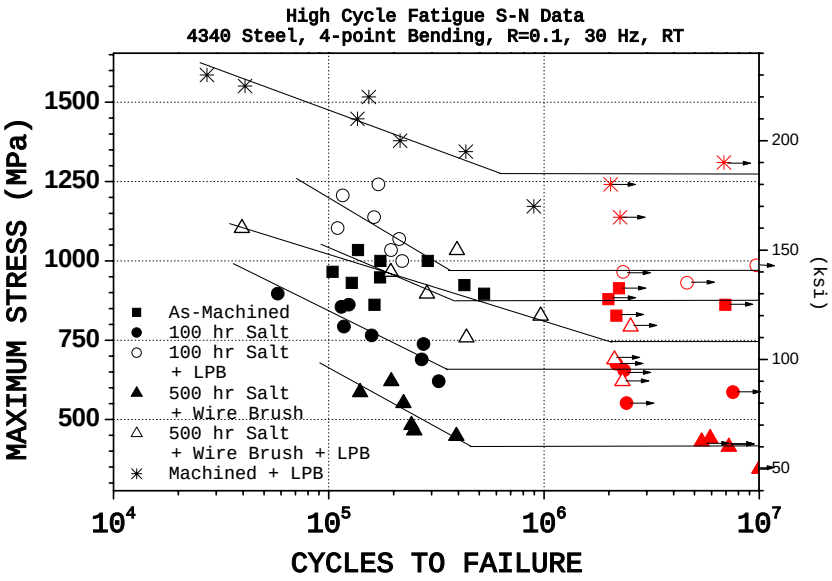

Figure 3 – HCF S-N plots of salt-fog exposed 4340 steel

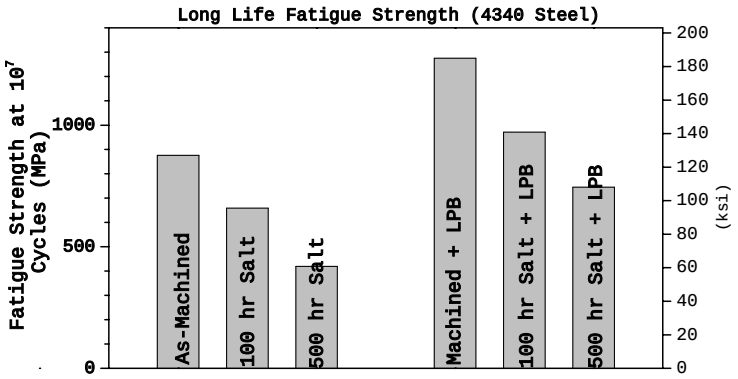

Figure 4 - Bar chart showing the relative fatigue strengths of salt-fog exposed 4340 steel

Fretting of 4340 steel produced a fretting scar in the form of a narrow band of black oxidation on the surface nominally 1 mm (0.04 in.) wide, but varying with the applied stress and strain range. The depth of the fretting scar was shallow, insufficient to remove the surface marks left by grinding. The width of the fretting scar was dependent upon the strain range of the test because the fretting was generated by a pad clamped to the surface of the cyclically strained fatigue sample. Fatigue cracks initiated from the edges of the scars at the point of maximum shear stress under contact loading.

The fretting fatigue results are shown in Figure 5. The ground baseline samples produced an endurance limit of 827 MPa (120.0 ksi). Fretting of as-ground samples during fatigue testing reduced the endurance limit to nominally 758 MPa (110.0 ksi). Pre-fretting followed by fretting during fatigue testing (simulating returning a fretted part to continued service) reduced the HCF endurance limit further to nominally 620 MPa (90.0 ksi), a loss of 25% of the initial fatigue strength.

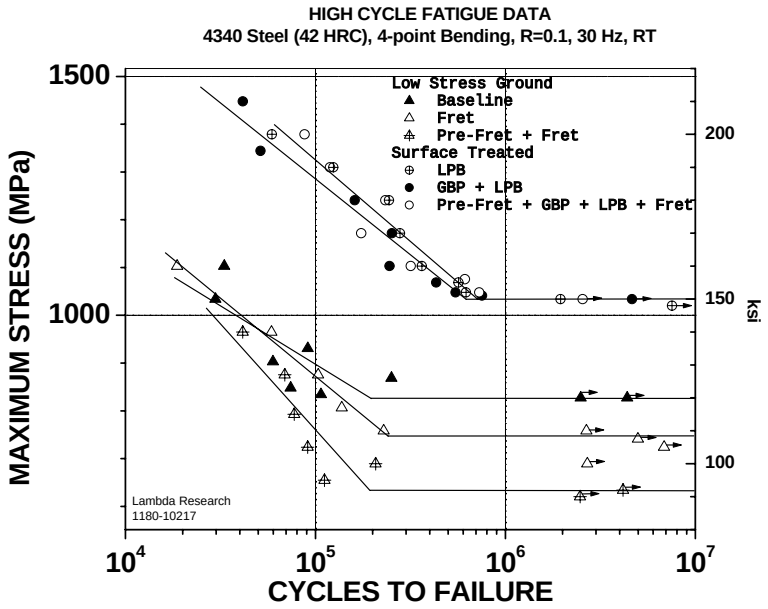

Figure 5 - 4340 steel fretting fatigue results

LPB, either before or after fretting, produced an endurance limit of nominally 1033 MPa (150.0 ksi), 25% higher than ground 4340 without fretting damage. Even with fretting, both before and after LPB, the LPB samples exhibited the same 25% endurance limit increase, indicating complete mitigation of the fretting fatigue debit.

Fatigue initiated from the edge of the fretting scar in all of the 4340 samples without LPB. Fatigue initiated in all LPB samples subsurface, just below the compressive layer, indicating a fatigue strength for the LPB surface even higher than indicated by the results achieved in bending. The subsurface failures are interpreted as a limitation of the test technique and sample design, which combined to allow the maximum tension to occur below the highly compressive test surface.

300M Steel

A comparison of residual stress profiles from shot-peened and LPB treated 300M HSLA steel specimens are shown in Figure 6. LPB treated specimens show compression to a depth of over 0.04 in. (1.2 mm) while the SP resulted in only 0.005 in. (0.1 mm) deep compression. In both cases, thermal exposure to 400ºF for 48 hours did not result in significant stress relaxation. A bar chart comparing the fatigue strengths of baseline material in the presence of a 0.01 in. (0.25 mm) deep FOD and/or active salt corrosion, with similar test conditions for shot peened and LPB treated specimens are shown in Figure 7. The results indicate both active salt corrosion and FOD decrease the fatigue strengths by a factor of 5, while the combined effects of FOD and active corrosion are even worse. SP has marginal beneficial effects when only active corrosion is considered, while no benefit is seen with the presence of FOD or with the combined presence of FOD and active corrosion. The results also indicate Ni-Cr plating had no benefit in mitigating corrosion fatigue damage. As seen in the LPB treated samples, almost all the damage from active salt corrosion, FOD, and the combined damage conditions are fully mitigated. The Ni-Cr plating on top of the LPB treated surface performed better than the shot-peened surface. Fractography indicated that all corrosion fatigue cracking damage initiated from corrosion pits. LPB did not stop the formation of corrosion pits, rather the crack initiation and growth processes were completely blocked by the deep compressive residual stresses. The Ni-Cr plating was

found to have numerous plating cracks, and corrosion pitting and SCC were not prevented by the plating process.

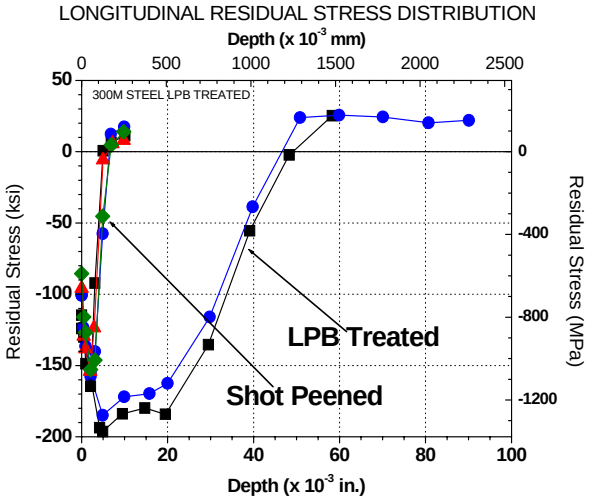

Figure 6 – Residual stress profiles of shot peened and LPB treated 300MHSLA steel specimens before and after 48 hours of thermal exposure to 400F

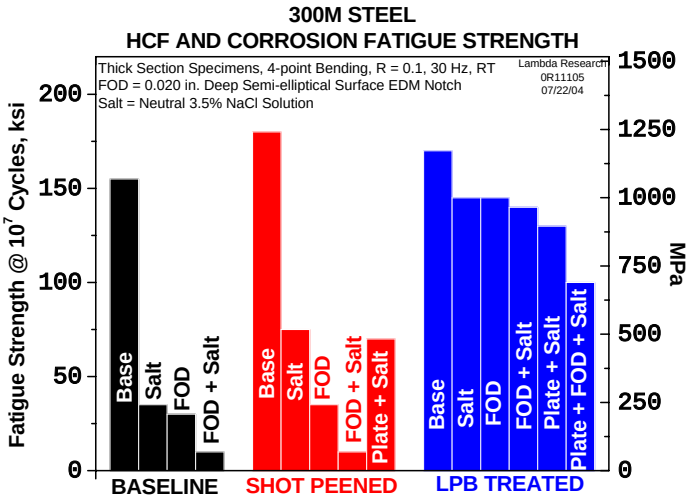

Figure 7 - Bar chart showing the fatigue strength of 300M HSLA steel

SCC studies on LPB treated 300M HSLA steel showed similar benefits. A bar chart of time to failure at different constant applied stresses on C-ring specimens is shown in Figure 7. Untreated baseline specimens, when stressed at 150 ksi, 165 ksi, and 180 ksi, failed after 261.8 hrs, 166.5 hrs, and 12.9 hrs respectively, of alternate immersion in neutral salt solution. The LPB treated specimens did not fail after 1,500 hrs of exposure. Efforts to increase the stresses beyond 180 ksi resulted in permanent bending of the LPB treated specimens, rather than failure. Thus, results indicate that LPB processing completely mitigated the SCC damage conditions in 300M HSLA landing gear steel.

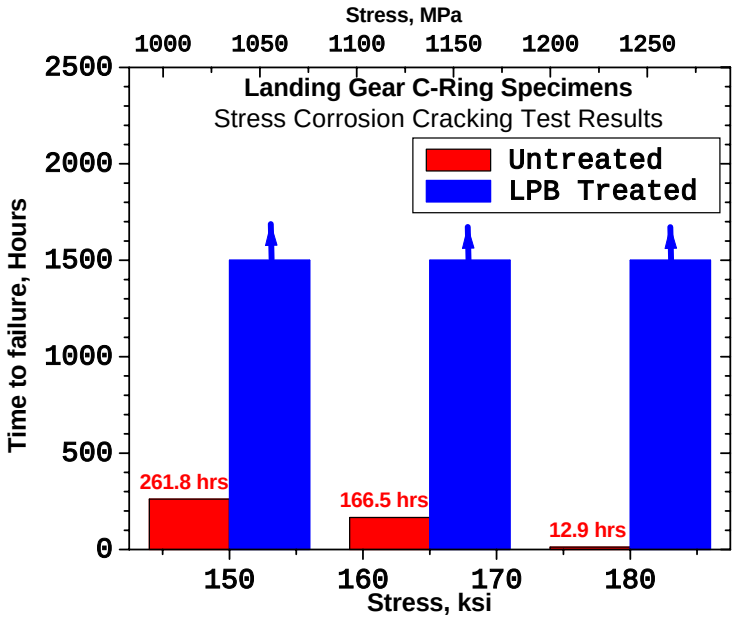

Figure 8 - SCC test results for 300M Steel

STRUCTURAL ALUMINUM ALLOYS

AA7075-T6

The pronounced fatigue strength reduction caused by salt pit corrosion or corrosion fatigue in a marine environment is well established for both steels[26,27] and aluminum alloys.[28] The fatigue strength debit for either mechanism is typically on the order of half the long-life, HCF endurance limit. Corrosion pits are a common site of fatigue crack initiation in the aluminum alloy 7075-T6 widely used for structural components of older aircraft. Pitting arises from intergranular corrosion to a depth dependent upon the service environment and the time of exposure, i.e., age of the aircraft. Current annual costs for corrosion inspection and repair of military aircraft alone are estimated to exceed one billion dollars. Currently, more than 30% of military aircraft are over 20 years old and over 90% are expected to exceed a 20-year life by the year 2015.[29] The total cost of ownership and fleet readiness are adversely affected. A means of mitigating corrosion and corrosion-related fatigue damage is needed.

The residual stress profiles of AA7075-T6 fatigue specimens in the as-machined and LPB treated condition are shown in Figure 9. A depth of compression of nearly 0.035 in. (0.9 mm) was achieved with LPB treatment. Figure 10 shows the HCF data for AA7075-T6 specimens tested in the as-machined and LPB treated conditions in both active corrosion mode as well as with prior salt-fog exposure. In the as-machined condition both active corrosion and prior salt-fog exposure results in a significant drop in the fatigue performance in that the fatigue strength at 10^7 cycles drop by 50% from about 32 ksi to 16 ksi. With LPB treatment the HCF properties are 50% higher than the as-machined condition. The results indicate the compressive residual stresses from LPB not only mitigated the corrosion pitting damage, but also far exceed the baseline performance.

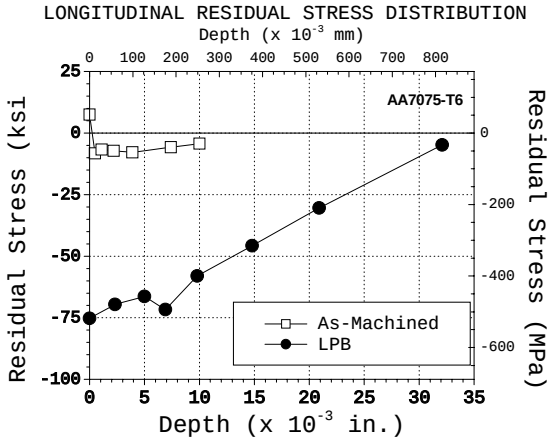

Figure 9 – Residual stress distribution in AA7075-T6 in the as-machined and LPB conditions

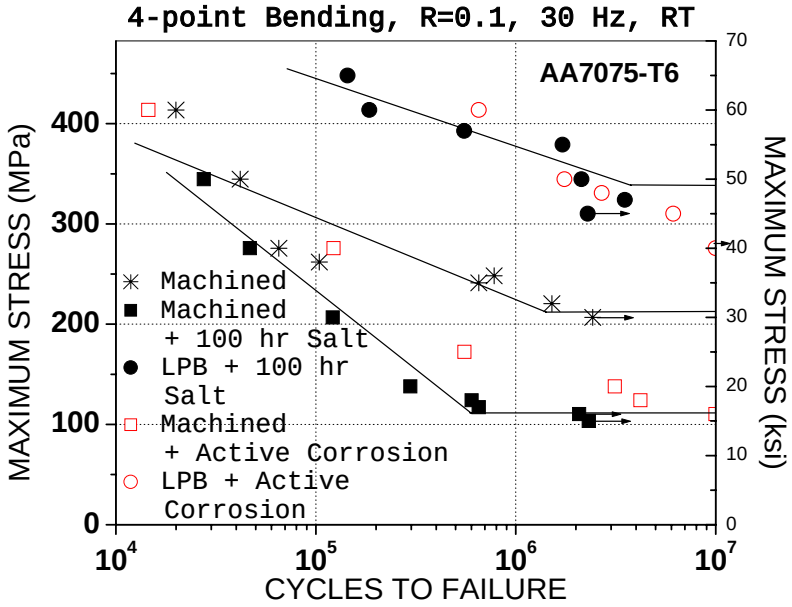

Figure 10 – HCF S-N data for AA7075-T6

AA2219-T8751

Friction stir welding (FSW) is emerging as a joining method for structural aluminum members. However, issues related to residual tensile stresses and surface finish lead to significant debit in fatigue performance. Test results indicate LPB has proven to be an excellent treatment by way of eliminating the tensile residual stresses, smoothing the surface to a mirror finish, and improving the fatigue performance, resulting in patented FSW applications.[30]

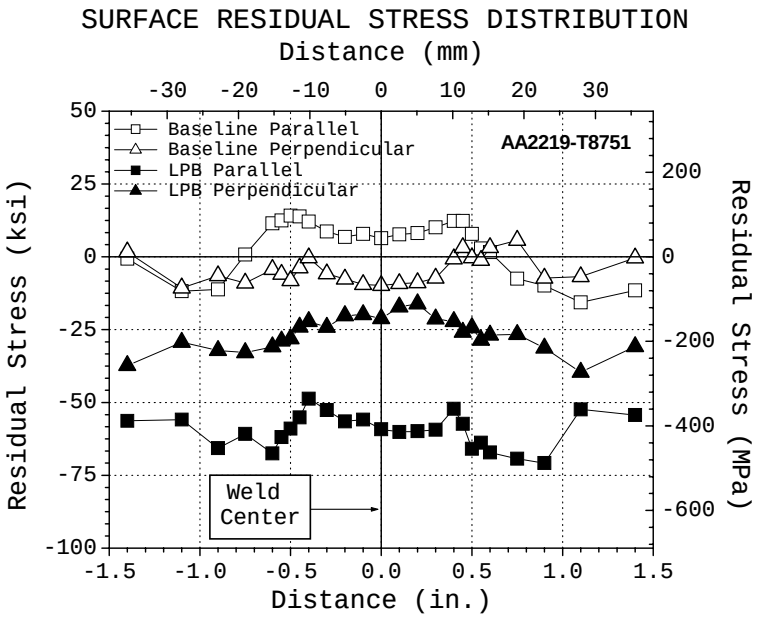

Figure 11 - Surface residual stress distribution in FSW plate AA2219-T8751

The residual stress distributions parallel and perpendicular to the weld on the surface of a friction stir welded plate of AA2219-T8751 are shown in Figure 11 for the as-welded condition and after LPB processing. As indicated in Figure 11, the surface tensile residual stresses created by the FSW process are completely eliminated and in place a compressive residual stress state is introduced by LPB treatment.

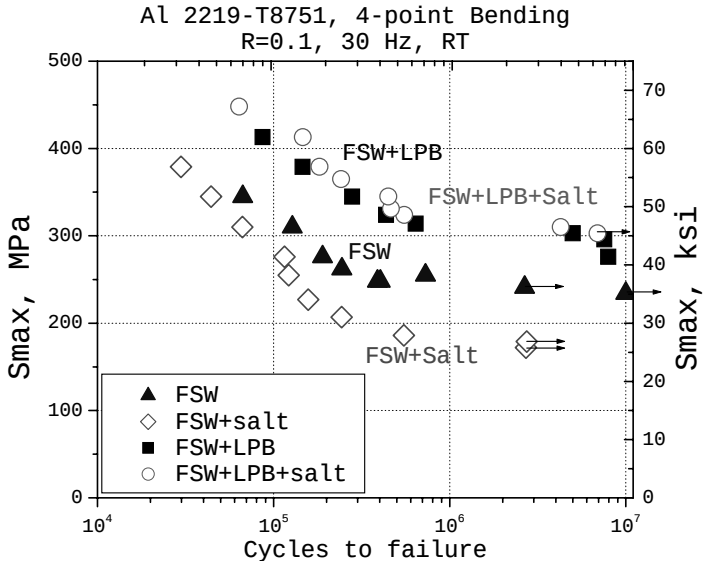

Figure 12 - HCF S-N plots for AA2219-T8751

A comparison of baseline FSW versus LPB treated FSW with and without active corrosion is shown in Figure 12. The fatigue strength of baseline FSW AA2219-T8751 is shown to decrease from nominally 35 ksi to 25 ksi in the presence of active corrosion. LPB treated FSW both in the baseline condition and the active corrosion conditions performed equally well and surpassed the performance of the baseline FSW. Improvement in the fatigue performance is evident at

nominally 45 ksi. This improvement is attributed to the surface compressive residual stresses seen in Figure 11.

CONCLUSIONS

LPB is shown to completely mitigate the tensile stress threshold dependent mechanisms of SCC and corrosion fatigue. LPB effectively mitigates the damage associated with fretting, pitting corrosion, and FOD in laboratory testing of structural aluminum alloys and steels. The deep compressive residual stress afforded by LPB effectively eliminates the damage growth process, although normal damage initiation mechanisms like fretting, pitting, rusting, etc., are still active. The effectiveness of LPB to mitigate damage in aircraft structural steels and aluminum alloys, has been demonstrated.

REFERENCES

1 Frost, N.E. Marsh, K.J. Pook, L.P., *Metal Fatigue*, Oxford University Press, 1974.
2 Fuchs, H.O. and Stephens, R.I., *Metal Fatigue In Engineerin*g, John Wiley & Sons, 1980.
3 Berns, H. and Weber, L., "Influence of Residual Stresses on Crack Growth," Impact Surface Treatment, edited by S.A. Meguid, Elsevier, 33-44, 1984.
4 Ferreira, J.A.M., Boorrego, L.F.P., and Costa, J.D.M., "Effects of Surface Treatments on the Fatigue of Notched Bend Specimens," Fatigue, Fract. Engng. Mater., Struct., Vol. 19 No.1, pp 111-117,1996.
5 Prevéy, P.S. Telesman, J. Gabb, T. and Kantzos, P., “FOD Resistance and Fatigue Crack Arrest in Low Plasticity Burnished IN718”, Proc of the 5th National High Cycle Fatigue Conference, Chandler, AZ. March 7-9, 2000.
6 Clauer, A.H., "Laser Shock Peening for Fatigue Resistance," Surface Performance of Titanium, J.K. Gregory, et al, Editors, TMS Warrendale, PA (1996), pp 217-230.
7 T. Watanabe, K. Hattori, et al, “Effect of Ultrasonic Shot Peening on Fatigue Strength of High Strength Steel,” Proc. ICSP8, Garmisch-Partenkirchen, Germany, Ed. L. Wagner, pg 305-310.
8 U.S. Patent 5,826,453 (Oct. 1998) and 6,415,486 B1 (Jul. 2002), other patents pending.
9 P. Prevéy, N. Jayaraman, R. Ravindranath, “Effect of Surface Treatments on HCF Performance and FOD Tolerance of a Ti-6Al-4V Vane,” Proceedings 8th National Turbine Engine HCF Conference, Monterey, CA, April 14-16, 2003
10 Paul S. Prevéy, Doug Hornbach, Terry Jacobs, and Ravi Ravindranath, “Improved Damage Tolerance in Titanium Alloy Fan Blades with Low Plasticity Burnishing,” Proceedings of the ASM IFHTSE Conference, Columbus, OH, Oct. 7-10, 2002
11 Paul S. Prevéy, et. al., “The Effect of Low Plasticity Burnishing (LPB) on the HCF Performance and FOD Resistance of Ti-6Al-4V,” Proceedings: 6th National Turbine Engine High Cycle Fatigue (HCF) Conference, Jacksonville, FL, March 5-8, 2001.
12 M. Shepard, P. Prevéy, N. Jayaraman, “Effect of Surface Treatments on Fretting Fatigue Performance of Ti-6Al-4V,” Proceedings 8th National Turbine Engine HCF Conference, Monterey, CA, April 14-16, 2003
13 Paul S. Prevéy and John T. Cammett, “Restoring Fatigue Performance of Corrosion Damaged AA7075-T6 and Fretting in 4340 Steel with Low Plasticity Burnishing,” Proceedings 6th Joint FAA/DoD/NASA Aging Aircraft Conference, San Francisco, CA, Sept 16-19, 2002
14 N. Jayaraman, Paul S. Prevéy, Murray Mahoney, “Fatigue Life Improvement of an Aluminum Alloy FSW with Low Plasticity Burnishing,” Proceedings 132nd TMS Annual Meeting, San Diego, CA, Mar. 2-6, 2003.
15 Paul S. Prevéy and John T. Cammett, “The Influence of Surface Enhancement by Low Plasticity Burnishing on the Corrosion Fatigue Performance of AA7075-T6,” Proceedings 5th International Aircraft Corrosion Workshop, Solomons, Maryland, Aug. 20-23, 2002.
16 John T. Cammett and Paul S. Prevéy, “Fatigue Strength Restoration in Corrosion Pitted 4340 Alloy Steel Via Low Plasticity Burnishing.” Retrieved from www.lambda-research.com Sept. 5, 2003.
17 Paul S. Prevéy, "Low Cost Corrosion Damage Mitigation and Improved Fatigue Performance of Low Plasticity Burnished 7075-T6", Proceedings of the 4th International Aircraft Corrosion Workshop, Solomons, MD, Aug. 22-25, 2000.

19 P. Prevéy, “The Effect of Cold Work on the Thermal Stability of Residual Compression in Surface Enhanced IN718,” Proc. 20th ASM Materials Solutions Conf. & Expo, St. Louis, MO, Oct. 10-12, 2000.
20 P. Prevéy, “The Measurement of Subsurface Residual Stress and Cold Work Distributions in Nickel Base Alloys,” Residual Stress in Design, Process & Materials Selections, ed. W.B. Young, Metals Park, OH: Am. Soc. For Metals, 1987, p 11-19.
21 P. Prevéy, P. Mason, D. Hornbach, & J. Molkenthin, “Effect of Prior Machining Deformation Upon the Development of Tensile Residual Stresses in Weld Fabricated Nuclear Components,” *Journal of Materials Engineering and Performance*, Vol. 5, 1, February 1996, p. 51-56.
22 P.S. Prevéy, Metals Handbook, Vol 10, ASM, Metals Park, OH, (1986), p. 380-392.
23 M.E. Hilley, ed, Residual Stress Measurement by XRD, SAE J784a, SAE, Warrendale, PA (1971)
24 Noyan & Cohen, Residual Stress Measurement by Diffraction & Interpretation, Springer-Verlag, NY, (1987)
25 P. Prevéy, W.P Koster, “Effect of Surface Integrity on Fatigue of Standard Alloys at Elevated Temperatures,” Fatigue at Elevated Temperatures, ASTM STP561, ASTM, Phil., PA, (1972)pp. 522-531.
26 ASM Handbook, Vol. 19, Fatigue and Fracture, S.R. Lampman, ed., ASM International, Metals Park, OH, 1996, pp. 596-597.
27 Cammett, J. and Prevéy, P., “Fatigue Strength Restoration in Corrosion Pitted 4340 Alloy Steel via Low Plasticity Burnishing,” (2001), Retrieved July 19, 2002, from http://www.lambda-research.com/publica.htm.
28 Dowling, N., Mechanical Behavior of Materials, Prentice Hall, NJ, 1993, p. 365.
29 Agarawala, V., "Corrosion and Aging: Aircraft Concerns," presentation at 11th Annual AeroMat Conference, Bellevue, WA, June 26-29, 2000.
30 U.S. Patent 6,926,970 B2 (Aug. 2005)

COMPOSITE PATCH DESIGN STUDY FOR EXTENSIVELY CORRODED WING PANELS LOADED IN COMPRESSION

G. Renaud, G. Li, G. Shi and M. Yanishevsky

Structures and Materials Performance Laboratory
Institute of Aerospace Research, National Research Council Canada
1200 Montreal Road, Ottawa, Ontario, Canada K1A 0R6

Abstract

Exfoliation corrosion is a major problem facing ageing transport aircraft fleets. The efficacy of composite repairs where the structure is primarily loaded in tension has been determined for many cases. However, for structures and components dominated by compression loading little actual test data are available. Extensive exfoliation corrosion damage caused by service environment exposure normally requires replacement of components, since rework would be well beyond normal repair limits. Large scale compression testing has been conducted at the NRC Institute for Aerospace Research to determine the ability of composite patch repairs to restore the residual strength of wing panels that have been reworked to 80% of their thickness. The compression tests were performed on representative extruded wing panels in three conditions: pristine, damaged, and damaged + repaired with composite patches. It was established that by using typical patch repair philosophy, where the lost area is rebuilt with boron patches of equivalent "stiffness × thickness", stresses were redistributed such that failure occurred prematurely in the repaired panel. Finite element (FE) modeling of the tests was carried-out to first determine whether the original test data could be reproduced analytically. Then a design parametric study process was undertaken to determine patch design aspects that are the most important to consider for restoring the residual strength of a damaged panel as close as possible to that in the pristine condition. Results obtained illustrate the modeling complexity associated with this problem and the importance of the chosen patch design in the repair performance. For example, results suggest that the application of a thicker patch on the inside surface of the panel may enhance the repair characteristics by reducing the bending field induced by the offset of the applied compressive loads.

Introduction

Exfoliation corrosion is a major problem facing ageing transport aircraft fleets. According to the typical “Find and Fix” philosophy, corrosion damage must be completely removed by grind-out during periodic and routine maintenance. Although most aircraft have allowable limits for such material removal, there are times where these limits must be exceeded to remove the corrosion completely. Conservative engineering judgment would have these structures replaced.

Bonded composite patch repairs are an option for some of these situations because they can be tailor designed to fit the grind-out area without requiring fasteners or additional holes being introduced in the structure. Composite doublers are also known to have good fatigue and corrosion properties. The efficacy of composite bonded patch repairs where the structure is primarily loaded in tension has been demonstrated for many cases. However, for structures and components dominated by compression loading, little actual test data are available.

In support to the United States Air Force (USAF) effort in Aircraft Corrosion Control and Coatings, tests were performed at the Institute of Aerospace Research (IAR) - National Research Council Canada (NRCC) to determine the ability of composite patch repairs to restore the residual strength of extensively corroded wing panels.

The test results showed unexpected behavior in terms of final failure loads, suggesting that the damage increased the compressive strength of the panels, while the repair decreased it. Patch post-cure thermal residual strains were identified as one possible cause for the early failure.

Detailed non-linear Finite Element (FE) analyses were performed to reproduce the test results, evaluate the proposed patch design, and provide additional understanding to improve the repair performance.

This paper will first describe the principal outcomes of the tests. The finite element models and results will be presented next, as well as some considerations on the effects of the post-cure thermal residual strains. Finally, results from a patch thickness design study will be given.

C-141 Wing Skin Compression Tests

Test Setup

Three C-141 lower wing panels with different damage characteristics (pristine, damaged, and damaged and patch-repaired) were tested in compression. The objective of these tests was to determine the ability of composite patch repairs to restore the residual strength of panels that have been reworked beyond their normal repair limits to eliminate exfoliation corrosion caused by service environmental exposure.

The test panels were removed from the aircraft and sectioned by Warner Robins Air Logistic Center (WRALC) staff and further machined at NRC. In addition, C-channel anti-buckling stiffeners were installed along the edges of the panel on the lower wing surface to simulate the support normally provided by adjacent wing panels, and to preclude premature failure because of unrepresentative buckling at the free edges. Fifty axial and rosette strain gauges, nine out-of-plane displacement transducers and one axial displacement transducer were installed on the panels. The dimensions and materials of this assembly are indicated in Figure 1.

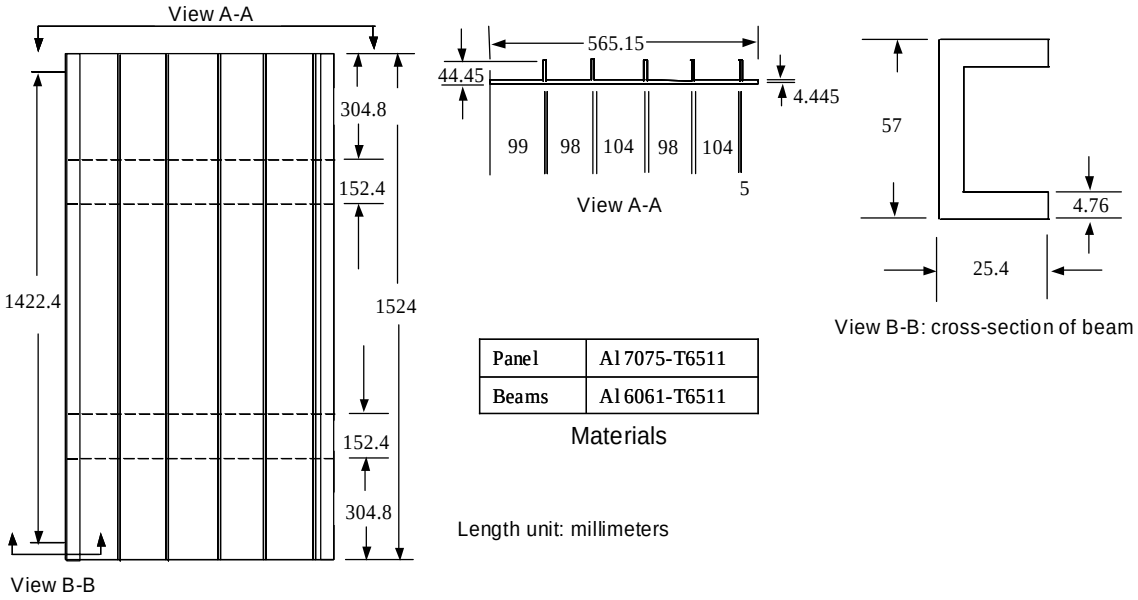

Figure 1. Basic panel configuration.

The first panel, with no apparent corrosion damage, was used for establishing the performance of the panel in the pristine condition. The second panel was used to establish the compressive strength of a "damaged" panel. It includes a centrally located milled "Z" (228.6 mm wide by 254 mm long, maximum depth of 80% of the panel thickness), as shown in Figure 2. The volume of material machined away simulated a worst-case scenario of what may be required to remove significant exfoliation or other corrosion damage and to address concerns about grind-outs affecting bending and torsional stability.

Figure 2. Centrally-Located Milled "Z" damage.

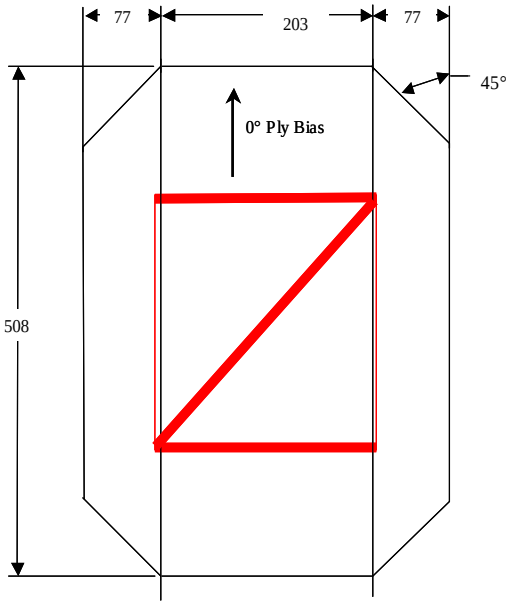

Figure 3. Patch Design on Panel Outer Surface.

The third panel was used to establish the compressive strength of a “damaged” panel with the same milled "Z" area as in the second tested but with boron composite patches installed on both sides of the panel. The repair was designed at WRALC using the results from a previous study [2] and the CRAS software [3,4]. The intent was to restore the compressive strength in the panel while limiting the strain in the groove and at the patch edge to prevent crack growth and minimize peel stresses in the adhesive. The patches were bonded to the panel with FM-73 adhesive and cured at 121 C. The same adhesive material was also used to fill the groove before repair application. The patch lay-up sequence is given in Table 1.

Ply	Angle	Material	Length
1	30°	Boron/Epoxy	508 mm
2	-30°	Boron/Epoxy	508 mm
3	-	FM-73	508 mm
4	15°	Boron/Epoxy	470 mm
5	-15°	Boron/Epoxy	470 mm
6	-	FM-73	470 mm
7	0°	Boron/Epoxy	445 mm
8	0°	Boron/Epoxy	432 mm
9	0°	Boron/Epoxy	419 mm
10	0°	Boron/Epoxy	406 mm

Table 1. Patch lay-up sequence.

The outer patch, shown in Figure 3, was built using 10 plies. The inner patch had the same overall design but used the first 8 plies only. Furthermore, it only covered the portions of the panel between the risers. The patch was received fully manufactured and bonded to the panel. No details on the CRAS software model or the predicted patch performance were provided.

Test Results

For the pristine panel, failure occurred when the forward riser buckled and separated from the inner skin. At that point, the other risers buckled and the lower wing skin buckled outward away from the risers. This catastrophic failure occurred at 1181 kN.

The damaged panel failed both forward & aft of the central risers. Unexpectedly, the damage made the panel able to carry a slightly higher load of 1200 kN prior to failure. The damage had the net effect of a cutout, such that the loading ended up being significantly better distributed over the entire cross-sectional area.

The repaired panel failed in a manner similar to the pristine panel. However, the addition of the patch repair resulted in a failure that occurred at 980 kN, significantly lower than the failure load of the other two panels. After failure, the boron patches were still fully bonded to the skins.

Considering the occurrence of yield strains in the panel, strain gauges measured that the bottom of the “Z” groove detected yield early in the load application for the damaged panel, at 402 kN. For the pristine and repaired panels, the first occurrence of yield was measured at the risers edge, in the central part of the panel. It should be noted however that no strain gauge was present in the groove for the repaired situation. Other strain gauges indicated that during

the bonding process which occurred in an autoclave at 121 C, the external skin had a high positive differential from the internal skin. This was considered likely to be responsible for encouraging premature buckling of the repaired panel. The failure data observed in the tests are summarized in Table 2.

Panel	Onset of Plasticity	0.2% Yield Strain	Final Failure
Pristine	1068 kN (risers)	1171 kN (risers)	1181 kN
Damaged	313 kN (Z groove)	402 kN (Z groove)	1200 kN
Repaired	757 kN (risers)	934 kN (risers)	980 kN

Table 2. Test failure data.

Finite Element Analysis

FE Model

Finite element models of the three panels were generated using MSC/Patran as the pre- and post-processor and MSC/Marc as the solver. The models used quadratic three-dimensional elements (Hex20, Wedge15, Tet10) for all components, and geometric nonlinearities (large strains and displacements) for the analysis. The panel and anti-buckling stiffener materials were considered non-linear, using the full stress-strain curve, the adhesive layer was assumed perfectly plastic and the patch was assumed elastic. The FE meshes for the panels are illustrated in Figure 4.

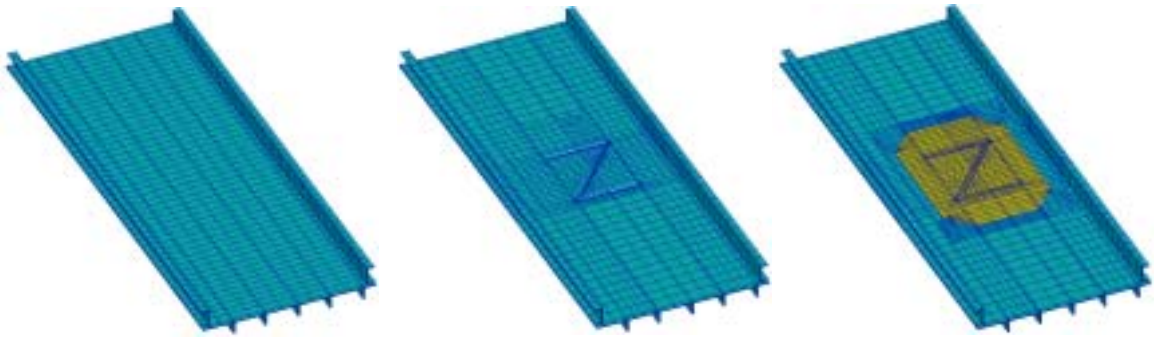

Figure 4. Finite element meshes for the panels.

Boundary conditions and multi-point constraints were imposed on the meshes to reproduce the test conditions. The bottom edge of the panel was fixed in all directions. The top edge was similarly restrained in the lateral and transverse direction. In addition, parts of the risers were also restrained in these directions to simulate the attachment to the rib supports. The load acting on the top edge was simulated by a single nodal force located at one node on the top edge and by multi-point constraints that forced uniform vertical displacement of the entire edge. Finally, links between the anti-buckling stiffeners and the panel were specified in the lateral and transverse directions only. This condition was set to simulate the slotted bolt holes used in the test to restrict any axial load transfer between these components. The test compression loading fixture and the equivalent boundary conditions and multi-point constraints are shown in Figure 5 and 6, respectively.

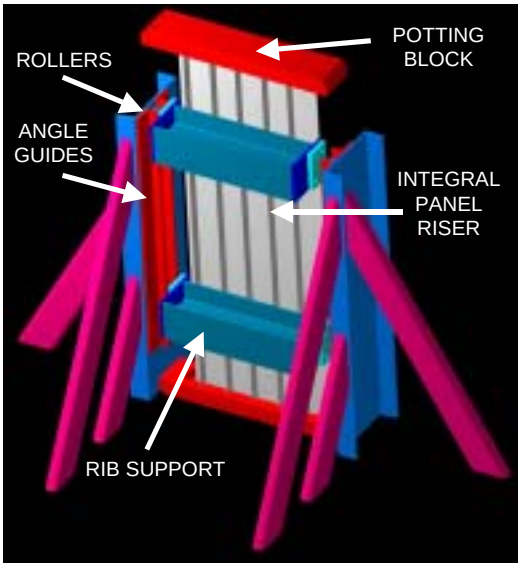

Figure 5. Compression loading fixture.

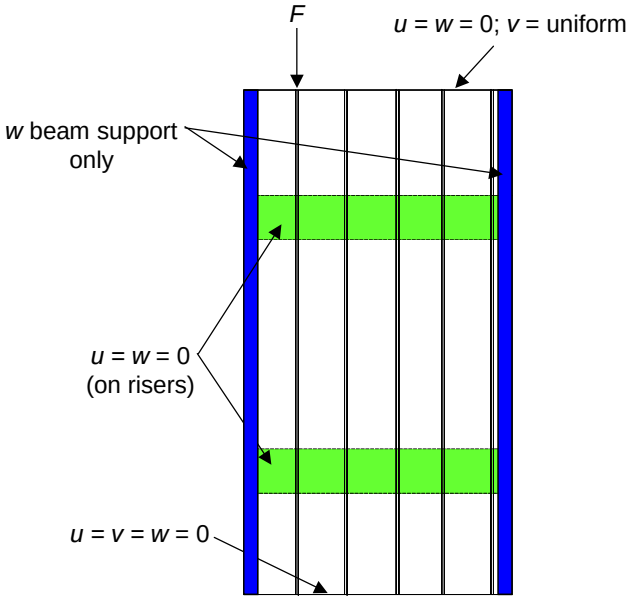

Figure 6. Boundary conditions and multi-point constraints.

A thermal load case was set-up to simulate the post-cure process for the repaired panel analysis. This initial step, preceding the post-buckling nonlinear analysis, consisted of a linear analysis with ΔT = -100 C. Boundary conditions were specified to solely prevent rigid body motions during and after the cure. Instead of forced zero displacements, the post-cure resulting lateral and transverse displacements were used as the boundary conditions involving those terms in the subsequent post-buckling analysis.

FE Results

Analysis results show good agreement between the model and the test for the pristine panel case. The displacement-force relationship observed in the test and in the simulation is shown in Figure 7.

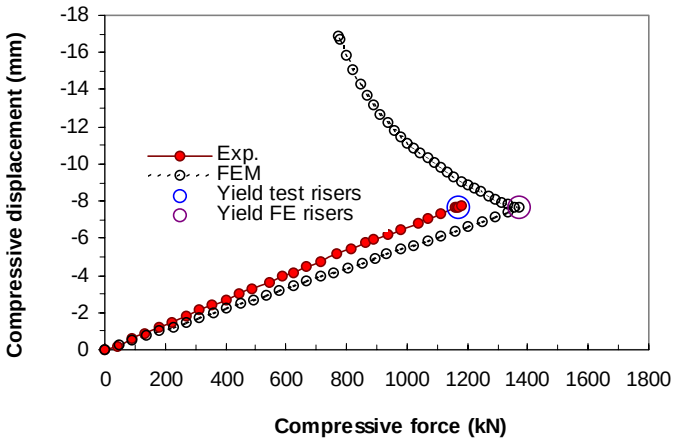

Figure 7. Displacement versus force (pristine panel).

It can be seen that, although the model has a higher axial stiffness and predicts a higher failure load, the overall behaviour of the FE model was similar to the test panel. In both the test and simulation the panel failed just after the first occurrence of yielding could be measured in the central risers, indicating that the panel failed after the central risers buckled.

The damaged panel simulation also captured the overall phenomena that occurred in the test. However, the model predicted, as intuition would suggest, a failure load lower than that observed in the pristine case. The displacement-force relationship for this case is shown in Figure 8.

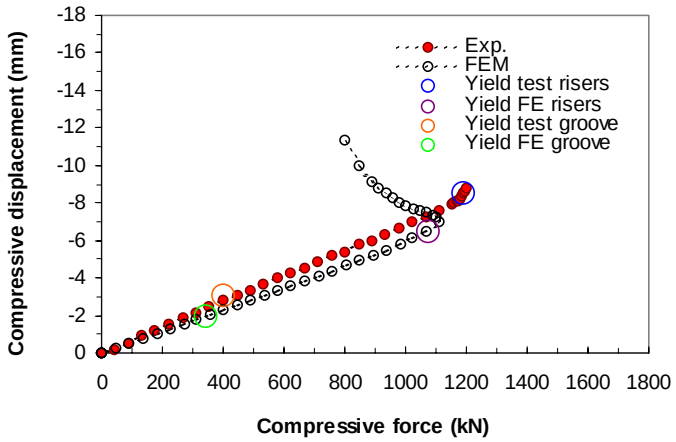

Figure 8. Displacement versus force (damaged panel).

Although yielding in the "Z" groove occurred early in the process, it can be seen that the final failure occurred, as for the pristine case, just after yielding was detected in the risers.

For the repaired panel, the modeled post-cure displacements and strains were found to be consistent with strain measurements obtained from the gauges installed prior to patching. In particular, the patches were put into a state of initial compression, and, conversely, the patched portion of the panel was put into a state of initial tension. This initial state of strain was expected because of low coefficient of thermal expansion of the patch material, which restrained the panel from returning to its initial state upon cooling. Furthermore, the center of the assembly slightly bulged outward, inducing a bending field putting the edges of the central risers in an initial state of compression.

However, the FE model did not reproduce all aspects of the tested repaired panel behavior. As for the damaged case, and contrary to what was observed in the test, the model predicted the expected behavior, that is the patch would restore the panel compressive strength, as planned by the patch designer using CRAS. The displacement-load relationship for the repaired panel is shown in Figure 9.

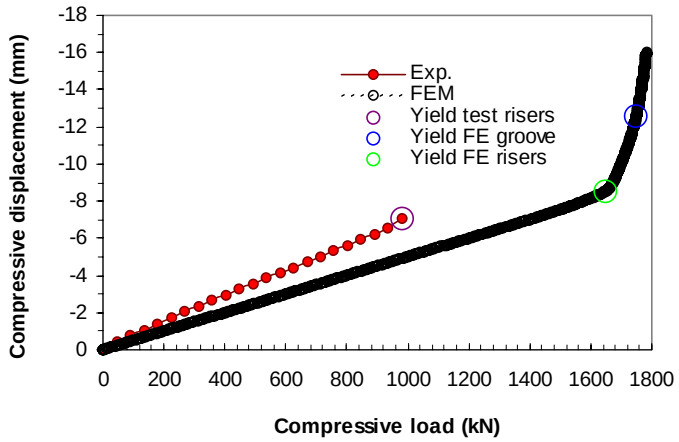

Figure 9. Displacement versus force (repaired panel).

As for the other cases, riser yielding triggered the final failure. In this case however the material in the "Z" groove did not yield before the panel entered its post-buckling state. Since there was no strain gauge installed in the groove, it was not possible to confirm that this phenomenon also occurred in the test. Adjacent strain gauge data however indicated that the strain in the patched area of the panel was significantly reduced.

Several factors may have contributed to the discrepancy between the modeling and test results. First, the material properties, especially the patch and adhesive properties were not fully provided. Furthermore, differences were observed between the design and actual manufactured patch provided to NRC. It is therefore not certain that the model considered the exact design of the patch in the test. Another probable cause of discrepancy is the choice of composite patch lay-up sequence. As seen in Table 1, the third and sixth plies of the laminate were made of adhesive material. More investigation should be conducted to determine the effects that these "soft" inner plies had on the patch performance, i.e. to what extent they actually contribute to load reduction in the panel. The post-cure thickness of these added adhesive plies is not known and may influence the axial and bending stiffness of the laminate. The FE model assumed that the adhesive plies remained unchanged upon manufacturing. It is probable that the CRAS model utilized the same assumption.

Other possible causes of the discrepancy could come from the test itself. For example, an unaccounted load eccentricity could have been present during the test.

Effects of Cure

To evaluate the effects of the post-cure residual strains, the repaired panel test was simulated without the post-cure step and compared to the analysis including the thermal effects. Some of the key characteristics of the two simulations are compared in Figures 10 and 11.

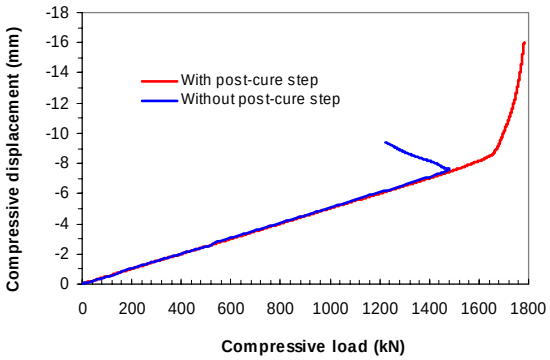

Figure 10. Effects of cure step on force-displacement relationship.

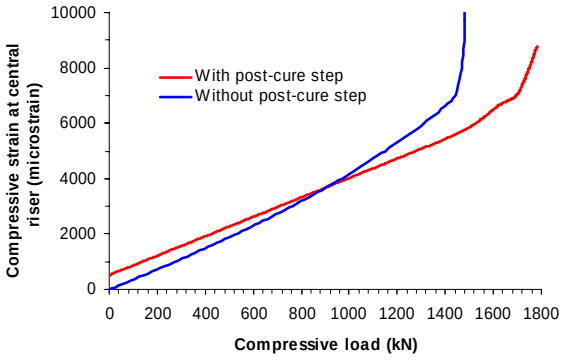

Figure 11. Effects of cure step on central riser strain.

It can be seen from Figure 10 that, and contrary to what was presumed from the test results, the post-cure step increased the final failure load by about 12%. This can be explained by the initial tensile strain state present in the center of the panel that the applied compressive load had to overcome before buckling. In addition, the compressive strains in the risers reach yield values more slowly when post-cure effects are considered, as shown in Figure. This explains why, although there exists an initial state of compression in the risers, final failure occurs later in the process in the absence of post-cure analysis. For a panel that would fail at a load lower than 900 kN, the effect of the cure would be the reverse. This load is actually close to the load at which the repaired panel failed in the test.

Design Parametric Study

Although the repaired panel model did not compare well with the test results, a preliminary study was carried out to determine if the patch designs could be improved to increase the performance of the repair. This study also intended to gain a better understanding of why the patch in the test behaved poorly.

The number of plies in the inner and outer patches was considered as variables for the design study. All combinations of 1 to 10 plies for both patches were considered for the analysis of the cooling process and a compressive load of 980 kN (the load at which the repaired panel failed during the test). Because of the high number of simulations required, the analysis was assumed linear. The compressive strain present in the central riser after cure and after the 980 kN load application (including the post-cure strain) is shown in Figures 12 and 13. This strain value was chosen because it was directly related to final failure for all cases considered.

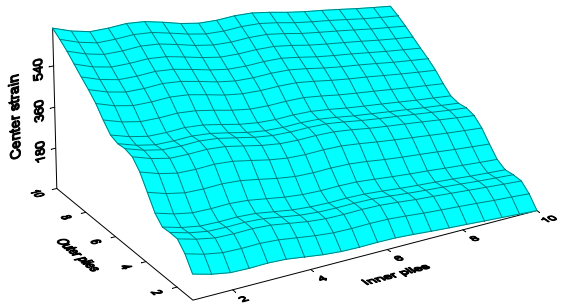

Figure 12. Effects of ply number on central riser post-cure strain (compressive microstrain).

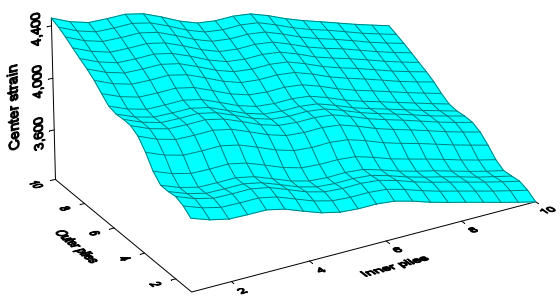

Figure 13. Effects of ply number on central riser strain (compressive microstrain) under 980kN compressive load, with post-cure.

It can be seen from Figure 12 that the central riser post-cure strain is almost independent of the number of plies in the inner patch. However, a thickness increase of the outer patch leads to higher post-cure compressive strains in the central riser. After the application of the load, it can be seen from Figure 13 that the best patch design to reduce the compressive strains in the central riser is a thin outer patch and a thick inner patch. Conversely, a patch that is thicker on the outer wing surface results in higher strains.

This design strategy to unbalance the repair, illustrated in Figure 14 for a single-sided patch, suggests that the system's neutral axis should be shifted inward, toward the risers to be more aligned with the loads.

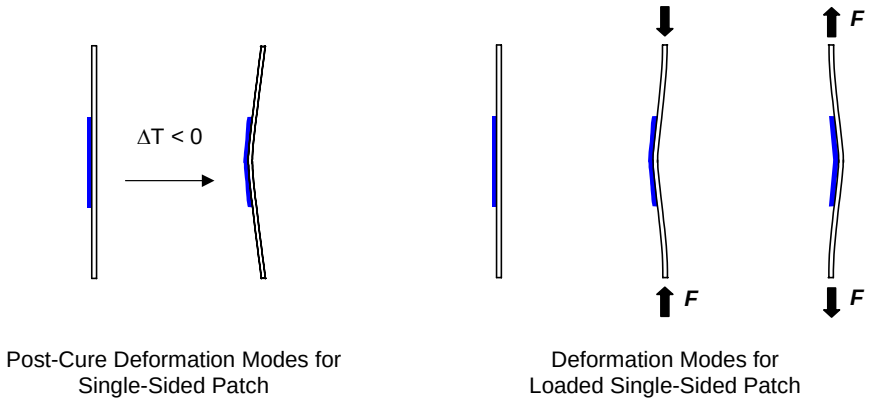

Figure 14. Bending effects of patch asymmetry.

If the panels illustrated in Figure 14 are patched on the riser side, it is seen that the resulting bending field would act against the load-induced bending. Indeed, since the loads are applied on the complete cross-sectional area of the panel (including the integral risers), the loading axis is located inward of the panel mid-surface. The provided design, consisting of 10 outer plies and 8 inner plies, implied a shift of the neutral axis in the opposite direction. This design, aiming at minimizing the strains in the damage, may have contributed to the early failure in the test by adding to the load-induced riser compressive strains.

Full non-linear analyses were performed on the "extreme" patch designs to verify the results obtained by the linear analysis parametric study. Table 3 presents the final failure load without the thermal effects and Figure 15 illustrates the failure load-displacement behavior differences with the thermal effects.

Number of plies	**Failure load (without cure)**
0 inner, 0 outer	1266 kN
0 inner, 10 outer	1419 kN
10 inner, 0 outer	1538 kN
8 inner, 10 outer (provided design)	1478 kN
10 inner, 10 outer	1485 kN

Table 3. Non-linear design study results – without post-cure simulation.

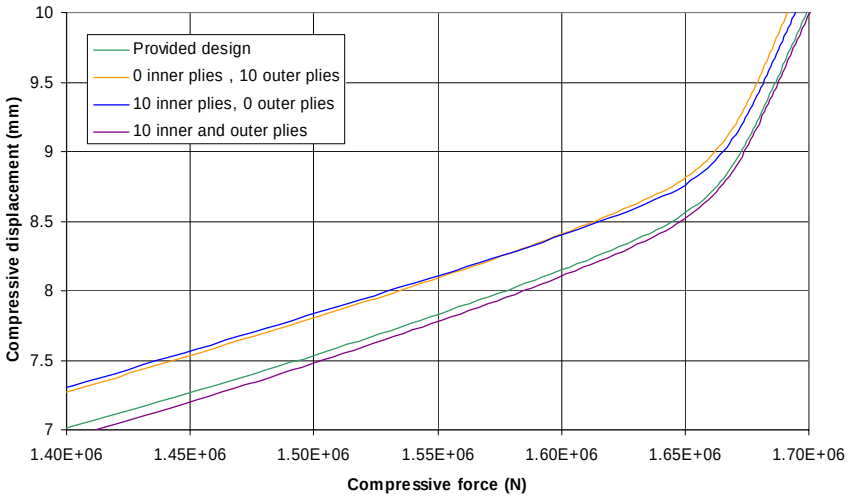

Figure 15. Non-linear design study results – with post-cure simulation.

The results show that with no patch, the failure load of the damaged panel predicted by the FE model is 1266 kN. This value is very close to the test value of 1200 kN (Table 1). It should be noted that this result is slightly better than the result presented in Figure 8 because the presence of the patch called for mesh refinement in the damaged area.

It is also seen in Table 3 that both single-sided cases (ten plies on one side, zero on the other), as well as the provided design, were able to increase the failure load when the thermal aspects of the problem were not considered. It is also shown, as suggested by the linear parametric study, that the best patch design implies more stiffening material on the inner surface that on the outer surface of the wing.

However, the results presented in Figure 15 show that the same conclusion cannot be drawn when the post-cure process simulation is included in the analysis. In this case the final failure load is difficult to identify but the curves suggest that the "10-10" patch would perform slightly better than the others. It should be noted that the differences in failure loads is very small among the various designs, suggesting that the residual thermal strains would make the various designs equivalent in terms of failure load. The stiffening effect of the repair is however different from one patch design to the other, as seen in the linear portion of the curves that show that the pre-buckling overall compression stiffness of the assembly is directly related to the total number of plies.

Conclusions

Three C-141 wing panels with different damage characteristics were tested in compression. Assuming a yield failure criterion, the pristine panel performed best, and the damaged panel performed worst. However, in terms of final failure, the damaged panel carried the most compressive load while the repaired panel carried the least. The central risers failed first in the pristine and repaired panels, leading to catastrophic failure. The "Z" damage encouraged the load to bypass the central risers in the absence of a repair. Strain gauge measurements indicated that the patch caused a very large gradient between the lower surface of the outer patch and the top of the riser, encouraging early riser buckling and riser / inner skin failure.

Finite element analysis results suggested a different ordering in the panel performances. Assuming both yield and final failure, the repaired panel gave the best results and the damaged panel the worst, contrary to what was observed in the test, especially for the repaired case. Possible causes of this discrepancy include the patch material properties, lay-up sequence, and manufacturing process, which could have been different and/or less efficient in the test than in the model.

A numerical post-cure effects investigation suggested that the tensile thermal residual strains might increase the final failure load and modify the post-cure behavior. This observation is different from the usual case where the post-cure strains are harmful because they are added to applied tensile loads. Linear and non-linear patch design parametric studies suggested that the patch should shift the assembly neutral axis inward, which would be more aligned with the loads. Results showed that the thickness of the patching material on the inner surface should be higher than on the outer surface. This was the configuration present in the provided repaired test panel. This conclusion can however not be made for the non-linear cases that included the post-cure simulation.

As future work, an investigation on the discrepancy between test and finite element results, particularly for the repaired configuration, should be carried out. In particular, the patch should be cut and its cross-section inspected to verify the documented ply lay-up (number and type of plies, and thickness). Furthermore, studies and optimizations concerning other patch parameters, such as ply angles, taper angle, size, and shape should be considered. An optimal design would have the riser yield load, seen as the driving force for the final failure, equal to the groove yield load and also equal to the pristine riser yield load. Finally, different patch design concepts could be explored. An example of an alternative concept would be a patch spanning the riser skin interface, going up the side of the risers.

Acknowledgements

The authors appreciate the efforts of the following individuals for the success of this work: Bruce Shaver – load fixture conceptualization; John Rogers – load fixture design and testing; Jean Lalonde, Kyle Fisher and John Macmillan – assembly and test support; Dale Shane, Albert Luteyn, Andrew Bartlett and Eric Curran – test article machining and preparation; and David Backman, Michel Delannoy and Chick Wilson – instrumentation and data acquisition.

The test program was funded by NCI information Systems Inc Contract No.F09603-99-D-0200 Subcontract No.NCI_USAF_9192-006 in support of the USAF effort in Aircraft Corrosion Control and Coatings.

The analysis work was carried out under the internal project 46_QI0_20, Computational Structures Analysis, supported by the Institute for Aerospace Research, National Research Council Canada.

References

[1] M. Yanishevsky, D. Backman and J. Rogers, "Test Protocol - Compression Testing of "Pristine", "Z" Cutout "Damaged", and "Z" Cutout "Damaged and Repaired" C-141 Wing Panels, LM-SMPL-2004-0014, January 2004.

[2] B. Spigel, J. Buckingham and F. McMaster, "Application of Composite Doublers to Corrosion Grind-Out, SwRI Project No. 18.01072.200 Task B, August 2000.
[3] Composite Repair of Aircraft Structures (CRAS) Design Manual, The Boeing Company, 2001.
[4] Composite Repair of Aircraft Structures (CRAS) Software User's Manual, The Boeing Company, 2002.

Cross–Reference of JSSG 2006 Guidance with MIL-STD-1530C Requirements

Introduction

This pamphlet will assist one to find guidance in the Joint Service Specification Guide (JSSG) 2006 that directly pertains to specific MIL-STD-1530C requirements.

MIL-STD-1530C describes the USAF Aircraft Structural Integrity Program (ASIP) which defines the requirements for achieving structural integrity in USAF aircraft while managing cost & schedule risks through a series of disciplined, time-phased tasks. It provides direction to government personnel and contractors engaged in the development, production, modification, acquisition, and/or sustainment of USAF aircraft. Section 5 of MIL-STD-1530C presents detailed requirements for the ASIP tasks.

The JSSG 2006 establishes the joint structural performance and verification guidance for the airframe. This guidance is derived from operational and maintenance needs and apply to the airframe structure which is required to function, sustain loads, resist damage and minimize adverse operational and readiness impacts during usage for the entire service life. There are two primary sections of the JSSG 2006, these being sections 3 & 4. Section 3 provides requirements that allow tailoring to a particular system. Section 4, verification, provides guidance to verify the requirements have been met. To assist filling in the blanks, Appendix A contains requirement rationale, guidance and lessons learned.

This document provides a cross reference with the requirements within Section 5 of MIL-STD-1530C to the applicable JSSG 2006 criteria to provide specific guidance for the particular MIL-STD-1530C requirement. Within the JSSG 2006, there was only one requirement that could not be cross-referenced to MIL-STD-1530C. This requirement was from section 3.2.23 (Lightning Strikes and Static Charge).

Authors:

POC:

David Keller, ASC/ENFS, WPAFB
David.Keller@wpafb.af.mil, (937) 255- 3330

Co-Authors:

David Bushroe, ASC/ENFS, WPAFB
Eric Bucher, ASC/ENFS, WPAFB
John Bailey, ASC/ENFS, WPAFB
Adam Yingling, ASC/ENFS, WPAFB
Hsing Yeh, ASC/ENFS, WPAFB
Faustino Zapata, ASC/ENFS, WPAFB
Irving Schaff, ASC/ENFS, WPAFB

ASIP Standard 5.1 - Design Information (Task I)

Section (MIL-STD-1530C)	MIL-STD-1530C Title	Referenced JSSG Section(s)	JSSG Title
5.1	Design information (Task I)	3.17 *	Engineering Data Requirements
5.1.1	ASIP Master Plan	None	
5.1.2	Design service goal and design usage	3.2.14	Service Life and Usage
5.1.3	Structural design criteria	3.1, 3.3, 3.8, 3.9 *	Design Requirements
5.1.3.1	Loads criteria	3.2 (except 3.2.19-21, 23, 25-30), 3.4	General Parameters, Structural Loading Conditions
5.1.3.2	Dynamics criteria	3.5, 3.6, 3.7	Aeroacoustic Durability, Vibration, Aeroelasticity
5.1.3.3	Strength criteria	3.10	Strength
5.1.3.4	Durability criteria	3.2.26, 3.11, 3.14	Maintainability, Durability, Sensitivity Analysis
5.1.3.4.1	Onset of Widespread fatigue Damage (WFD)	3.11.1	Fatigue Cracking /Delamination Damage
5.1.3.4.2	Economic life	3.2.30, 3.11, 3.14	Cost Effective Design, Durability, Sensitivity Analysis
5.1.3.5	Damage tolerance criteria	3.12	Damage Tolerance
5.1.3.5.1	Damage tolerance design concepts	3.12	Damage Tolerance
5.1.3.5.2	Special applications	3.12, 4.12, 3.15	Damage Tolerance, Force Management
5.1.3.6	Mass properties criteria	3.2.5, 3.2.6	Weights, Center of Gravity
5.1.4	Durability and damage tolerance control program	3.13	Durability & Damage Tolerance Control Plan
5.1.4.1	Durability and damage tolerance control plan	3.13	Durability & Damage Tolerance Control Plan
5.1.4.2	Critical part/process selection and controls	3.1.3.1	Parts Classification
5.1.5	Corrosion prevention and control program (CPCP)	3.11.2	Corrosion Prevention and Control
5.1.5.1	Corrosion prevention and control plan	3.11.2	Corrosion Prevention and Control
5.1.5.2	Evaluation of corrosion susceptibility	4.11.2	Corrosion Prevention and Control
5.1.6	Nondestructive inspection program	3.11.6	Nondestructive testing and inspection (NDT/I).
5.1.7	Selection of materials, processes, joining methods, and structural concepts	3.2.19, 3.10.1, 3.10.2, 3.10.4.3, 3.10.4.4, 3.16 *	Materials
5.1.7.1	Stability	3.2.19, 4.2.19, 4.16	Processes
5.1.7.2	Producibility	3.2.25, 4.2.25, 4.16	Producibility
5.1.7.3	Inspectability	3.11.6	Nondestructive testing and inspection (NDT/I)
5.1.7.4	Mechanical and physical properties	3.2.19, 4.2.19	Materials
5.1.7.5	Supportability	3.2.20, 4.2.20, 3.2.21, 4.2.21, 3.2.26, 4.2.26, 3.2.27, 4.2.27, 3.2.28,4.2.28, 3.2.29, 4.2.29	Maintainability, Supportability, Repairability
5.1.7.6	Risk mitigation actions	None	

* Includes these JSSG paragraphs in addition to what is listed under the sub-requirements.

ASIP Standard 5.2 - Design Analysis and Development Testing (Task II)

Section (MIL-STD-1530C)	MIL-STD-1530C Title	Referenced JSSG Section(s)	JSSG Title
5.2	Design analyses and development testing (Task II)	4.17*	Engineering Data Requirements Verification
5.2.1	Material and joint allowables	3.2.19, 4.2.19, 4.10.4.3, 4.10.4.4, 4.16	Materials and Processes
5.2.2	Loads analysis	4.2 (minus 4.2.19-21, 23, 25-30), 4.4.a	General Parameters, Structural Loading Conditions (Analyses)
5.2.3	Design service loads spectra	3.2.14.6, 3.2.14.7	Design Durability Service Loads/Spectrum, Design Damage Tolerance Service Loads/Spectrum
5.2.4	Design chemical/thermal environment spectra	3.2.16, 3.11.3	Chemical, Thermal, and Climatic Environments, Thermal Protection Assurance
5.2.5	Stress analysis	4.10	Stresses and Strains
5.2.6	Damage tolerance analysis	4.12	Damage Tolerance
5.2.7	Durability analysis	4.11.1.1, 4.14	Analyses, Sensitivity Analysis
5.2.7.1	Onset of Widespread Fatigue Damage (WFD)	4.11.1	Fatigue Cracking /Delamination Damage
5.2.7.2	Economic life	4.2.30, 4.11, 4.14	Cost Effective Design, Durability, Sensitivity Analysis
5.2.8	Corrosion assessment	4.11.2	Corrosion Prevention and Control
5.2.9	Sonic fatigue analysis	4.5.1.1	Aeroacoustic Durability Analyses
5.2.10	Vibration analysis	4.6.1	Vibration Analyses
5.2.11	Aeroelastic and aeroservoelastic analysis	4.7.a, 4.7.1-5	Aeroelasticity (Analyses)
5.2.12	Mass properties analysis	3.2.5, 3.2.6, 4.2.5, 4.2.6	Weights, Center of Gravity
5.2.13	Survivability analysis	4.8, 4.9	Required structure survivability (nuclear, nonnuclear)
5.2.13.1	Vulnerability analysis	4.8, 4.9	Required structure survivability (nuclear, nonnuclear)
5.2.13.2	Weapons effects analysis	4.8, 4.9	Required structure survivability (nuclear, nonnuclear)
5.2.14	Design development tests	4.2.19, 4.4.b, 4.5.1.2.1.1, 4.6.2.1, 4.7.b, 4.7.c, 4.10.4.3, 4.10.5.1, 4.11.1.2.1	Development tests
5.2.14.1	Duration of durability tests	4.11.1.2.2	Durability Tests
5.2.14.2	Corrosion tests	4.11.2, 4.2.19.1	Corrosion Prevention and Control, Materials
5.2.15	Production NDI capability assessment	3.11.6, 4.12.1	Nondestructive testing and inspection (NDT/I), Flaw sizes
5.2.16	Initial risk analysis	N/A	

* Includes these JSSG paragraphs in addition to what is listed under the sub-requirements.

ASIP Standard 5.3 Full-Scale Testing (Task III)

Section (MIL-STD-1530C)	MIL-STD-1530C Title	Referenced JSSG Section(s)	JSSG Title
5.3	Full-scale testing (Task III)	4.17*	Engineering Data Requirements Verification
5.3.1	Static tests	4.10.5.2, 4.10.5.6, 4.10.6 *	Static Strength
5.3.1.1	Selection of test article	4.10.5.2	Static Strength
5.3.1.2	Schedule requirement	4.10.5, 4.10.7, 4.10.8	Static Strength
5.3.2	First flight verification ground tests		
5.3.2.1	Mass properties tests	3.2.5, 3.2.6	Weights, Center of Gravity
5.3.2.2	Functional proof tests	4.10.5.3, 4.10.5.5	Functional proof tests prior to first flight.
5.3.2.3	Pressure proof tests	4.10.5.4, 4.10.5.5	Strength and pressurization proof tests.
5.3.2.4	Strength proof tests	4.10.5.4, 4.10.5.5	Strength and pressurization proof tests.
5.3.2.5	Control surface rigidity and free play tests	4.7.c, 4.7.4	Aeroelasticity (Laboratory Tests), Free Play of control surfaces and tabs
5.3.2.6	Ground vibration tests	4.6.2.2, 4.7.c, 4.7.d	Ground Vibration Tests, Aeroelasticity (Laboratory Tests), Aeroelasticity (Air Vehicle Ground Tests)
5.3.2.7	Aeroservoelastic tests	4.7.d, 4.7.2	Aeroelasticity (Air Vehicle Ground Tests), Aeroservoelasticity
5.3.3	Flight tests		
5.3.3.1	Flight and ground loads survey	4.4.c, 4.4.1, 4.4.2, 4.10.7, 4.10.8	Structural Loading Conditions (Flight and Ground Tests), Flight Loading Conditions, Ground Loading Conditions, Initial and interim strength flight releases, Final strength flight releases
5.3.3.2	Dynamic response tests	4.4.c, 4.4.1, 4.4.2, 4.10.7, 4.10.8	Structural Loading Conditions (Flight and Ground Tests), Flight Loading Conditions, Ground Loading Conditions, Initial and interim strength flight releases, Final strength flight releases
5.3.3.3	Flutter tests	4.7.e, 4.7.1, 4.7.2	Aeroelasticity (Air Vehicle Flight Tests), Aeroelastic Stability, Aeroservoelasticity
5.3.3.4	Aeroacoustic tests	4.5.1.2.2	Ground and Flight aeroacoustic measurements
5.3.3.5	Vibration tests	4.6.2.3	Ground and flight vibration measurements
5.3.4	Durability tests	4.11.1.2.2	Durability Tests
5.3.4.1	Selection of test article	4.11.1.2.2.a	Durability Tests
5.3.4.2	Test scheduling and duration	4.11.1.2.2.b & .f	Durability Tests
5.3.4.3	Inspection program	4.11.1.2.2.e	Durability Tests
5.3.4.4	Teardown inspection and evaluation	4.11.1.2.2.e & c	Durability Tests
5.3.5	Damage tolerance tests	4.12	Damage Tolerance
5.3.6	Climatic tests	4.2.16	Chemical, thermal, and climatic environments.
5.3.7	Interpretation and evaluation of test results	4.4.c, 4.4.1, 4.4.2, 4.7.e, 4.5.1.2.2, 4.6.2.3, 4.7.1, 4.7.2, 4.10.3, 4.10.4, 4.10.5, 4.10.7, 4.10.8, 4.11.1.2.2.c	

* Includes these JSSG paragraphs in addition to what is listed under the sub-requirements.

ASIP Standard 5.4 – Certification and Force Management Development (Task IV)

Section (MIL-STD-1530C)	MIL-STD-1530C Title	Referenced JSSG Section(s)	JSSG Title
5.4	Certification and force management development (Task IV)	4.17*	Engineering Data Requirements Verification
5.4.1	Certification analyses	4.4.c, 4.4.1, 4.4.2, 4.7.e, 4.5.1.2.2, 4.6.2.3, 4.7.1, 4.7.2, 4.10.3, 4.10.4, 4.10.5, 4.10.7, 4.10.8, 4.11, 4.12,	
5.4.1.1	Risk analyses	None	
5.4.1.2	Quantifying the accuracy of analyses	None	
5.4.2	Strength summary & Operating Restrictions (SSOR)	3.10.7, 4.10.7, 3.10.8, 4.10.8	Interim and Final Strength Flight Release
5.4.3	Force Structural Maintenance Plan (FSMP)	3.15, 4.15	Force Management
5.4.3.1	Structural maintenance database development	3.15	Force Management
5.4.3.2	Inspections	3.2.14.5	Airframe Structure Inspection
5.4.3.2.1	Inspection intervals	3.12.2	Residual Strength and Damage Growth Limits
5.4.3.2.2	Inspection methods	3.11.6	Nondestructive Testing and Inspection (NDT/I)
5.4.3.3	Surveillance	3.15, 4.15	Force Management
5.4.3.3.1	Analytical Condition Inspection (ACI) program	None	
5.4.3.3.2	Structural teardown program	4.12	Damage Tolerance
5.4.3.4	Repair criteria	3.2.28, 4.2.28, 3.12.2, 4.12.2	Repairability, Residual Strength & Damage Growth Limits
5.4.4	Loads/Environment Spectra Survey (L/ESS) development	3.15, 3.15.1	Force Management, Data Acquisition System Provision
5.4.5	Individual aircraft tracking (IAT) program development	3.15, 4.15	Force Management
5.4.5.1	Tracking analysis method	3.15, 4.15	Force Management
5.4.6	Rotorcraft Dynamic Component Tracking (RDCT) program development.	None	

* Includes these JSSG paragraphs in addition to what is listed under the sub-requirements.

ASIP Standard 5.5 – Force Management Execution (Task V)

Section (MIL-STD-1530C)	MIL-STD-1530C Title	Referenced JSSG Section(s)	JSSG Title
5.5	Force management execution (Task V)	4.17*	Engineering Data Requirements Verification
5.5.1	Individual aircraft tracking (IAT) program	3.15.1, 4.15	Data Acquisition System Provisions, Force Management
5.5.2	Rotorcraft dynamic component tracking (RDCT) program development.	None	
5.5.3	Loads/environment spectra survey (L/ESS)	4.15	Force Management
5.5.3.1	Initial loads/environment spectra survey	3.15, 4.15	Force Management
5.5.3.2	Loads/environment spectra survey updates	3.15, 4.15	Force Management
5.5.4	ASIP manual	None	
5.5.5	Aircraft structural records		
5.5.5.1	Structural maintenance records	3.15, 4.15	Force Management
5.5.5.2	Weight and balance records	3.2.5, 3.2.6	Weights, Center of Gravity
5.5.6	Force management updates	3.15, 4.15	Force Management
5.5.6.1	Durability and Damage Tolerance Analysis (DADTA) and IAT program updates	4.15	Force Management
5.5.6.2	Corrosion assessment updates	3.11.2, 4.11.2	Corrosion Prevention and Control
5.5.6.3	Risk analysis updates	None	
5.5.7	Recertification	All paragraphs previously identified for sections 5.1-5.4 of MIL-STD-1530	

* Includes these JSSG paragraphs in addition to what is listed under the sub-requirements.

Developing Guidelines for Bonded Repair of Stress Corrosion Cracking and the Application of X-ray Diffraction Residual Stress Mapping Technology to Aerospace Structures

M. Brauss[1], J. Pineault[2], M. Yanishevsky[3], J. Eiblemeier[4] and D. Stargel[5]

1) Michael Brauss, President, Proto Manufacturing Limited, 2175 Solar Crescent, Oldcastle, ON, Canada, N0R 1L0, Telephone: (519) 737-6330 Facsimile: (519) 737-1692, proto@protocol.com

2) James Pineault, XRD Laboratory Director, Proto Manufacturing Limited, 2175 Solar Cr., Oldcastle, ON, Canada, N0R 1L0, Telephone: (519) 737-6330 Facsimile: (519) 737-1692, xrdlab@windsor.igs.net

3) Marko Yanishevsky, Ph.D., Research Officer, Structures, Materials and Propulsion Laboratory, National Research Counsel of Canada, 1200 Montreal Rd., Building M-14, Ottawa, ON, Canada, K1A 0R6, Telephone: (613) 991-6926, Marko.Yanishevsky@nrc-cnrc.gc.ca

4) Josef Eiblmeier, Ph.D., Aerospace Group Manager, Martec Ltd., 717 St-Joseph Blvd., Suite 101, Gatineau, PQ, Canada, J8Y 4B8, Telephone: (819) 595-3526 Facsimile: (819) 595-1739, josef@martec.com

5) David Stargel, Ph.D., Aerospace Engineer, Air Force Research Laboratory, Air Vehicles Directorate (AFRL/VASM), 2790 D Street, Bldg 65, WPAFB, OH, 45433, Telephone: (937) 904-8779 DSN 674-8779, david.stargel@wpafb.af.mil

INTRODUCTION

Aluminum alloys such as 7075-T6 and 7079-T6 were used extensively on several military aircraft around the world, including the C-130, KC-135, C-141, C-5 and P-3, and several commercial aircraft, such as the Boeing 707, 727, 737 and 747. At the time these aircraft were designed, these alloys seemed an excellent choice since they combined the high strength and low density then required by the designers. For all their advantages, however, many of the "7000" series aluminums are susceptible to various forms of corrosion, including stress corrosion cracking (SCC). SCC is insidious and difficult to detect, while also presenting unique challenges for repair. Presently, structural components are either repaired by grinding out the identified cracks or replaced. Replacement of a structural member can be extremely costly due to the high number of man-hours required, and as a result, alternative methods for repair are being investigated. The USAF and commercial aviation have been interested in developing guidelines for the application of bonded repair (BR) technology to the SCC problem.

Stress Corrosion Cracking (SCC)

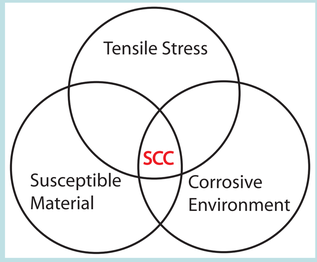

XRD used to determine the Residual Stresses

FEA MODELING

A SCC repair is successful if the repair prevents growth of the SCC damage and restores the strength or stiffness of the damaged structure to the pre-damage condition. The bonded patch repair has to protect the SCC susceptible surfaces from the environment and/or reduce the sustained surface tensile stress below the SCC threshold without increasing the surface stress outside the bonded patch beyond the SCC threshold.

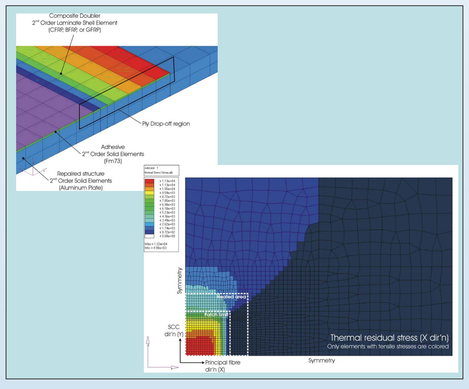

Finite element analysis was used to evaluate and compare over 405 bonded patch repair configurations (boundary condition stiffness, double material, patch lamination sequence, ply orientation, adhesive thickness, drop-off configuration, cure temperature) to determine the lowest post-cure thermal residual stresses in the direction of interest for SCC. As expected, the boundary condition stiffness and the doubler material are the parameters that have the most leverage on the induced thermal residual stresses, contributing to approximately 66% of the response.

SCC COUPONS

The objectives of the SCC Pilot testing were to:

- Determine whether or not damage due to SCC would continue to grow under zero or positive sustained load when the 3.5% NaCl bulk environment was excluded (effect of residual environment at the crack tip).
- Determine if there was a positive performance change in terms of residual strength compared to previous accelerated SCC data.
- Develop any necessary counter-measures.

14 SCC specimens from an NCI Al 7075 T6511 extrusion were subjected to two levels of pre-stress (20 and 30 ksi) and exposed to a 3.5% NaCl solution in an alternate immersion tank for two days in accordance with ASTM G 139. The specimens were then removed and cleaned with deionized water, dried with nitrogen gas, and stored in an environmental chamber set at 21°C and 30% relative humidity. Residual strength break load tests followed by SEM fractographic analysis were conducted at 0, 2, 5, and 19 days following alternate immersion testing. Results indicate that the progression of SCC had been arrested. The link between environment and load appears to have been successfully broken to prevent continued SCC by the cleaning and isolation process.)

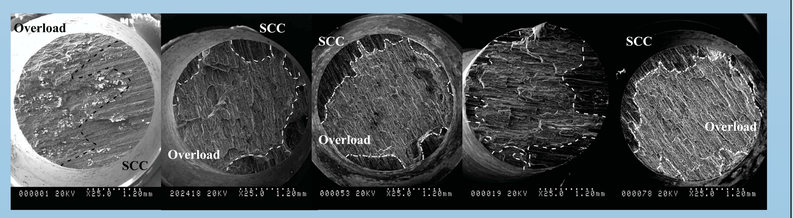

Premature failure | 2 days | 4 days | 7 days | 21 days

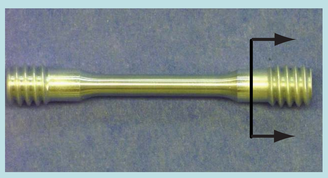

LT plane cross section

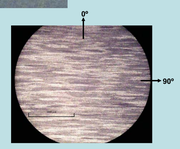

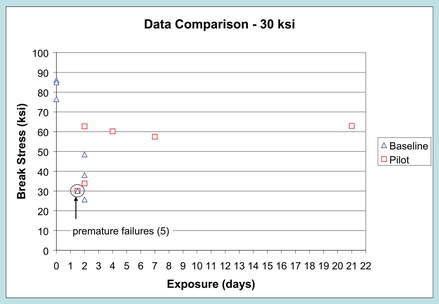

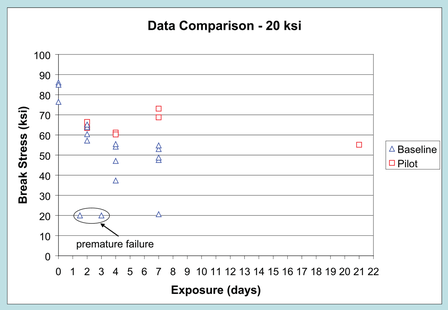

IMPROVED BONDED PATCH DESIGN AND RESIDUAL STRESS MEASUREMENT

The parameters that drive the design of bonded repairs in a metal fatigue scenario are well known and documented. There has been at least one documented effort to apply bonded repair technology to structures damaged by SCC, however, this effort raised a number of issues that are not addressed by the traditional methods of designing bonded repairs and that have remained unanswered to this day:

1. The level of residual/residential stress present in the damaged structure.
2. Impact of residual/residential stress on design for SCC damage.
3. Re-exposure to corrosive environment.
4. Geometry of target components.

X-ray diffraction (XRD) is desirable for use in RS measurement because it is a non-contact, nondestructive method with high spatial resolution and accuracy. Traditionally, there have been difficulties with the practical measurement of RS on airframe components in the field using XRD. Modern XRD equipment is rapid, highly portable, light-weight, rugged and flexible enough to access locations of interest on airframes.

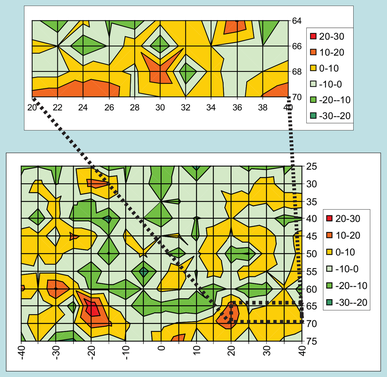

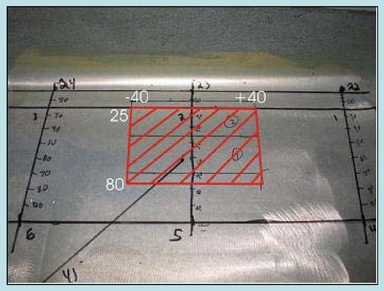

DEVELOPING GUIDELINES FOR BONDED REPAIR OF STRESS CORROSION CRACKING

The key for efficient SCC bonded patch repair is to minimize the induced thermal residual stresses under and beside the repair, while providing an effective and durable environmental barrier to prevent further damage. An optimal SCC patch repair design includes information from the microstructure analysis and XRD residual stress measurements, which are essential to identify the SCC susceptible area (exposed short-transverse grains associated with sustained surface tensile stresses). These results will allow designing more efficient bonded composite patches for fatigue enhancement or fatigue repair.

The combination of proven stress measurement technology and advanced modeling tools now provide an opportunity for verifying and quantifying the impact that these issues may have on the repair process. In the event that they do, the analytical data supported by meaningful coupon test data should provide a sound basis for establishing revised design guidelines.

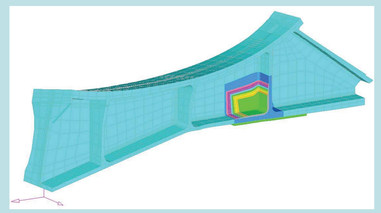

Disassembly and Inspection of C-5A 69-0004 Subsections

J. Suzel (S&K Technologies, Inc.)
1Lt Greg Koch (WR-ALC / LTES) - Government Lead Engineer

HQ AMC is funding a multi-year project managed by the 330th Strategic Airlift Sustainment Group to perform a structural teardown and inspection of a retired C-5A aircraft (S/N 69-0004) to gain a better understanding of the present condition of the airframe.

S&K Technologies, Inc. (SKT) is providing component management and inspection support for the program in cooperation with the Lockheed Martin (LMAS), AFRL and the other team members.

This poster paper will focus primarily on SKT's role.

Team Members

- WR-ALC / LTES – Program Lead
- Lockheed Martin
- AFRL/MLSA
- 653rd CLSS
- USAFA
- WR-ALC / ENFM
- S&K Technologies
  - Battelle
  - Cessna
  - Epps Aviation
  - MERC
  - NIAR
  - Northrop Grumman
  - SAIC
  - SwRI
  - UDRI

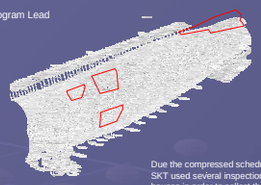

Due the compressed schedule, SKT used several inspection houses in order to collect the data in time for a thorough review by LMAS, the C-5 SPO and AFRL. All inspection houses were pre-qualified by an AF lead IPT.

Constraints/Challenges

- Compressed Schedule
- Magnitude of Task
- Large & Diverse Team
- Environmental & Safety
- Evolving Requirements
- Logistics
- Program Control
- Weather
- Fuel Tank Coating Removal
- Part Etching & EVI

SKT supported the teardown by providing heavy equipment such as cranes, safety and support equipment, photo documentation, special tooling and even cables to tie down the aircraft as hurricane Jeanne approached.

Program Phases:

- Phase I – "Quick Look"
- Phase II – Teardown and Inspection Work Package Development (IWP)
- Phase III – Inspections and Analysis
- Phase IV – Demolition & Scrapping of Teardown Article

LMAS is tasked to develop the IWPs, perform the analysis and make recommended changes to the C-5 maintenance and inspection plans.

A database was developed by SKT to manage the flow of work, relay requirements, track progress, allow for real-time oversight and provide for a warehouse to store the massive amount of data collected.

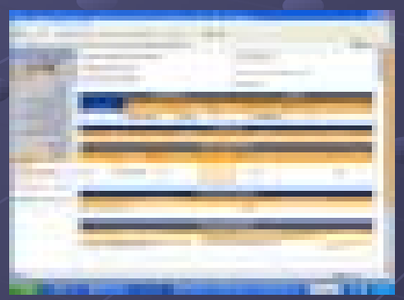

Finding information is uploaded into the database by the inspection lab creating a permanent, searchable library detailing the damage found and allowing for immediate review and disposition by LMAS and the IPT.

SKT provided expertise in the area of aircraft teardown, component disassembly and extraction of metallurgical specimens.

Since the C-5 is such a large aircraft, performing a full, exhaustive structural teardown of the entire aircraft was not feasible. Therefore, a prioritization system was developed by an IPT to select which sections of the aircraft would be evaluated. Areas of the aircraft were selected and ranked based on several factors:

- Fatigue test findings
- Inspection regime
- Degree of structural failsafety
- Inspection difficulty
- Structural capability
- Complexity of corrective action

Non-Destructive and Destructive Inspections

Primary Inspections:

- Visual
- Bolt Hole Eddy Current
- Eddy Current Surface Scan
- Fluorescent Penetrant
- Magnetic Particle Inspection
- Enhanced Visual

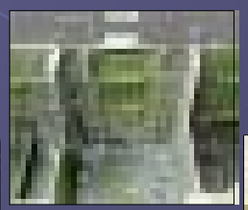

Secondary Inspections:

- Fractography
- Metallography
- Chemical Analysis
- Mechanical Property Analysis
- Ultrasonic Thickness Measurement
- Surface Corrosion Reparability Evaluation

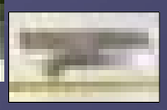

SKT coordinated the completion and documentation of all inspection results with technical oversight from AFRL.

Logistics Management

A key element of SKT's effort was the distribution and tracking of aircraft components:

- 73 major subsections (IWPs) extracted from A/C 69-0004
- IWPs weighed up to 1000 lbs each
- More than 7800 individual parts shipped & inspected
- Parts were distributed to 12 inspection labs and several processing facilities

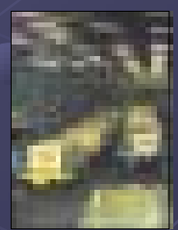

Finding Resolution

- Damage finding is entered in DB by Inspector IAW General Spec
- Lockheed reviews data and provides recommendation
- SPO and IPT reviews finding and recommendation - comments
- Lockheed writes MER if additional investigation warranted
- SPO & IPT reviews MER and modifies if required
- Finding is 'team approved' in DB Tracker by SKT
- Automated e-mail is generated for MERs initiating RFP
- Metallurgical Lab uploads report when complete
- Report is reviewed by IPT and approved in Tracker
- IWP is archived when actions on all findings and MERs are completed & approved by all IPT members

The C-5 Teardown Final Report will be completed in the summer of 2006.

S&K TECHNOLOGIES

Fatigue and damage tolerance analysis for correlation between loading type and service life of aging aircraft

Soonwan Chung
Koenraad Gieskes
Seungbae Park

Department of Mechanical Engineering
State University of New York at Binghamton

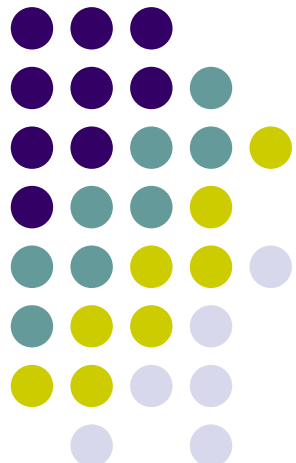

USAF ASIP 2005 (Aircraft Structural Integrity Program)

29 November – 1 December 2005
Memphis, TN

BINGHAMTON UNIVERSITY
State University of New York

Objectives

- To investigate the correlation between the load history and the service life of aging aircraft.

- To develop a systematic tool for service life extension and prediction by combining FE results, predicted load history and fatigue analysis

BINGHAMTON UNIVERSITY
State University of New York

Approach

- Model and analyze structural parts using finite element and maximum static loading
- Calculate the predicted fatigue life using various loading histories
- Compare the predicted fatigue life with of F-16 C/D SLEP (Service Life Extension Program)
- Find the effects of changes in load history on the predicted fatigue life

BINGHAMTON UNIVERSITY
State University of New York

Static FEA Model

- Two structural parts of F-16 C/D Aircraft
  - Dimensions and static loading used correspond to the F-16 SLEP study
  - Loading conditions

    Part 1: downward surface force at inner surface

    Part 2: combined in-plane force at circular hole

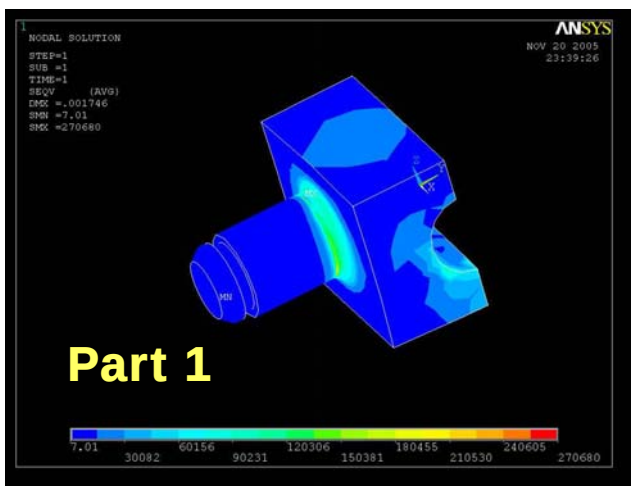

Von-Mises stress

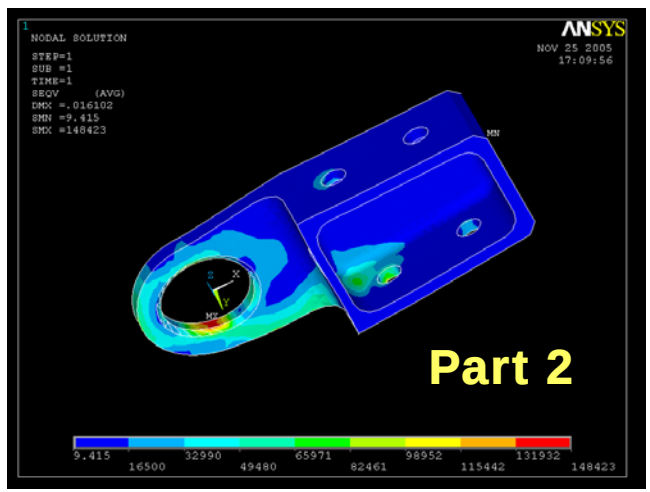

Load History Data - I

- Falstaff load history
  - Fighter Aircraft Loading STAndard For Fatigue evaluation
  - Standard load sequence for the load time history in the lower wing skin near wing root of a fighter aircraft
  - 200 mixed mission flights that means 35,966 numbers equally distributed over “peaks” and “troughs”
  - A uniquely defined sequence of numbers, ranging from 1 to 32, representing the subsequent peaks and troughs in load history

BINGHAMTON UNIVERSITY
State University of New York

Load History Data - I

- Full FALSTAFF
  - 200 Flights, 250 Hours, Avg. load = 12.9, STD Dev.=3.9

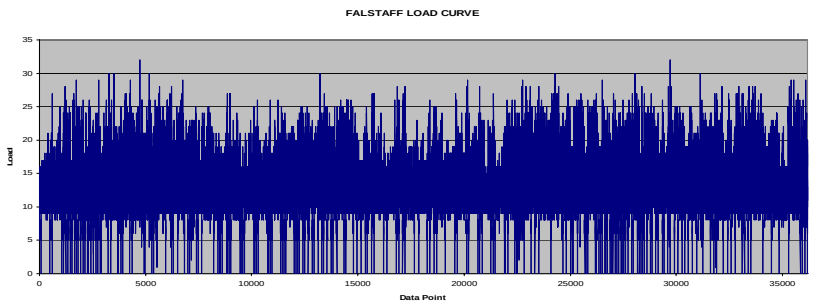

- 2nd Half FALSTAFF
  - 100 Flights, 125 Hours, Avg. load = 13.1, STD Dev.=3.9

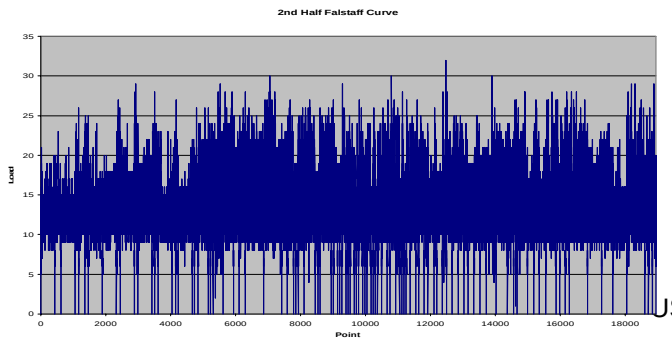

BINGHAMTON UNIVERSITY
State University of New York

Load History Data - II

: Random two-flight load history spectra based on FALSTAFF

- Two-flight FALSTAFF-1
  - 2 Flights, 5 Hours, Avg. load = 12.9, STD Dev.=4.0

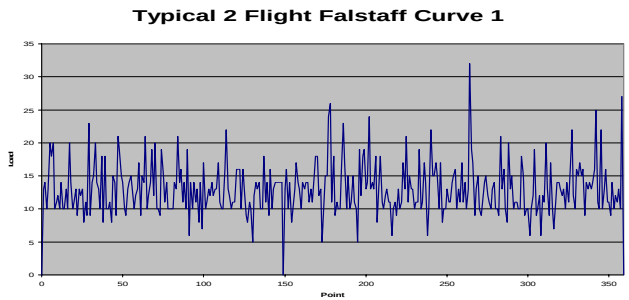

- Two-flight FALSTAFF-2
  - 2 Flights, 5 Hours, Avg. load = 12.9, STD Dev.=3.9

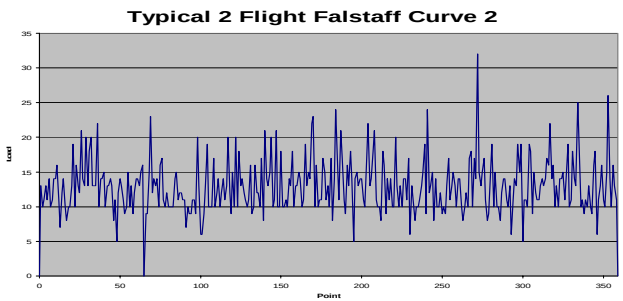

BINGHAMTON UNIVERSITY
State University of New York

Fatigue Model

- Fatigue life predictions
  - An initial crack is assumed
  - Crack growth curves are generated by MSC.Fatigue along with stress results

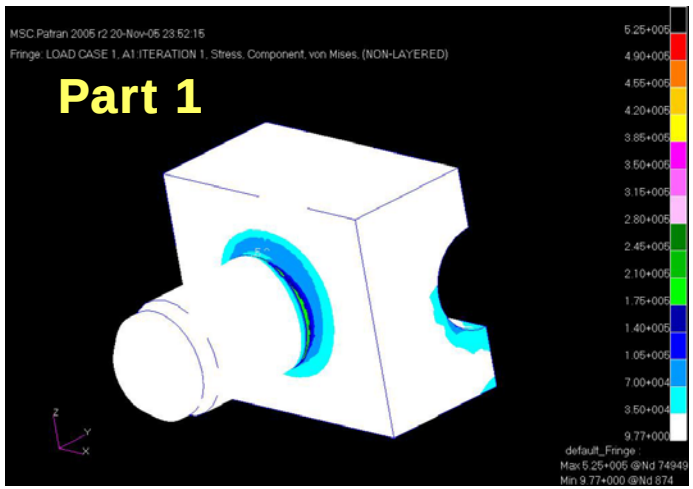

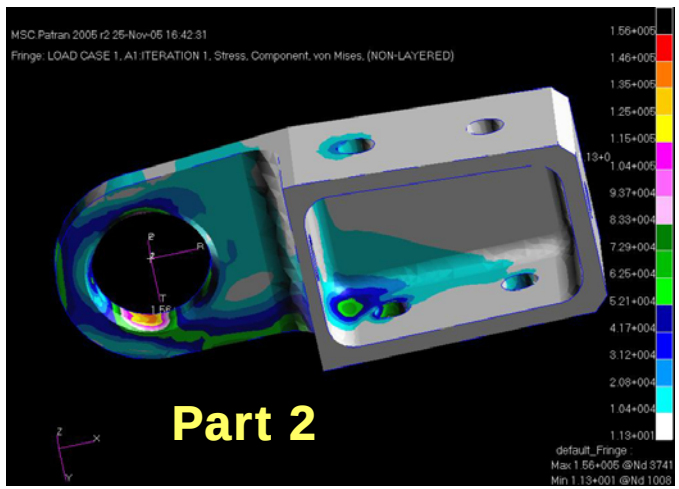

Crack Growth Data

- Part 1
  - Initial crack length = 0.005 in.
  - Final crack length = 0.019 in.
  - SLEP: 16,000 flight hours

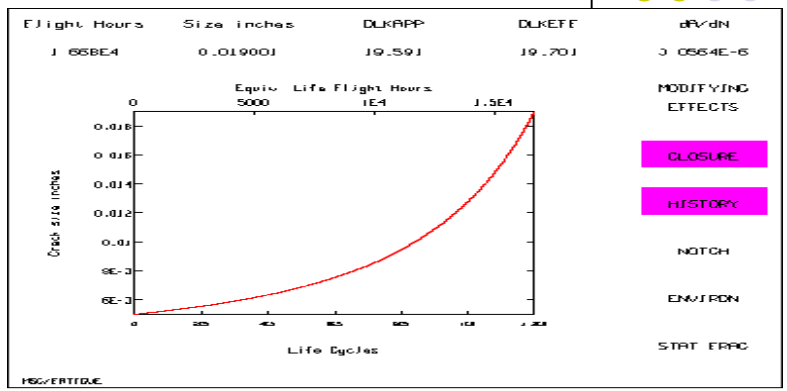

16P-1109 LC 1A, solid cylinder under bending, Full Falstaff

	Full FALSTAFF	2nd Half FALSTAFF	4th Quarter FALSTAFF	Two-Flight FALSTAFF-1	Two-Flight FALSTAFF-2	Two-Flight FALSTAFF-3
Flight hours	16,680	19,910	14,380	11,810	12,990	11,920
Error (%)	4.25	24.4	-10.1	-26.2	-18.8	-25.5

- Part 2
  - Initial crack length = 0.005 in.
  - Final crack length = 0.075 in.
  - SLEP: 3,400 flight hours

	Full FALSTAFF	2nd Half FALSTAFF
Final crack length	0.062 in.	0.066 in.
Flight hours	15,520	13,640

BINGHAMTON UNIVERSITY
State University of New York

Conclusions and Future works

- The loading history used in this study is based on FALSTAFF, and the resulting fatigue life can be acceptable for predicting service life.
- While load histories are often long and complicated spectra, it is possible to generate representative shorter spectra if care is taken to ensure consistent characteristics
- Further study on loading history of fighter and its application to control points variously distributed over the aircraft structure will be conducted.
- Optimal design by changing structural geometry to retard crack growth will be approached.

Impact Indicator Paint for Composites

Aircraft Structural Integrity Program Conference 2005

Bryan E. Koene[1], Martin Rogers[1], H. Wade Schlameus[2], James Oxley[2]

Funding provided by US Air Force SBIR Phase II Contract #FA8650-05-C-5043; Program Monitor Allison Jacques, WPAFB

***Abstract**: Luna Innovations has developed impact indicator paints for polymer matrix composites (PMCs) used as structural components in military and commercial aircraft. The impact indicator paint coated on a PMC will change color in response to an impact event capable of damaging the underlying composite. The impact indicator paint will allow aircraft maintenance personnel to rapidly identify potential composite damage in the field without the use of expensive equipment. Areas of damage highlighted by the paint can then be more closely inspected to determine needed repairs. The coating is able to qualitatively assess damage areas exceeding a threshold impact energy relevant for Low Velocity Impact Damage (LVID), as well as quantify the energy exerted onto the component through intensity measurements. Luna has incorporated this indicator additive into existing aircraft coatings, as well as new low volatile organic compound (VOC) coatings developed in house.*

Impact Indicator Paint Program Objective

Objective:
- Develop a graphite fiber composite damage detection method which improves rapidity, cost, and/or certainty of post-damage inspections

Luna's Approach:
- Demonstrate an impact indicator paint for fiber reinforced polymer composites used in military aircraft that will respond colorimetrically to an impact event capable of damaging the underlying composite

Requirements:
- Paint responds to impact at different impact levels i.e. different color change, different intensity of coloration
- Visibly observable from 6 ft away for maintenance personnel to spot potential damage
- Damage tolerance 1000-1500 inch·lb / inch (thickness) / inch^2
- Paint must not respond to impact below a certain level to avoid false positive e.g. maintenance crews working on aircraft without triggering mechanism

Composite Damage with Impact

- Panel below (1/16" Epoxy / carbon fiber composite) shows damage incurred with drop of 2 lb, ¼" diameter weight

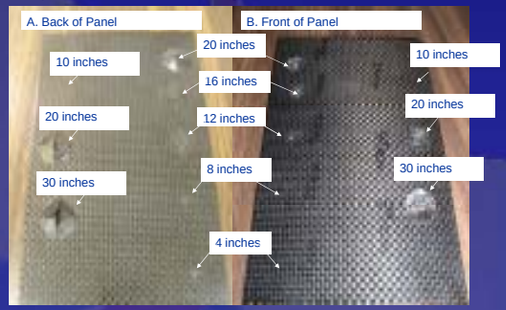

- Delamination is observed when weight is dropped below 4 inch height, but not observed on the front surface until greater than 3X the energy

Method of Operation of Luna's Impact Indicator Paint for Qualifying Impact Energy:

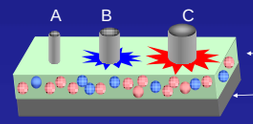

Visual Impact Demonstration

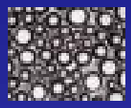

Microscopic Image of Microencapsulated Dyes

A. Light impact does not affect color change
B. Moderate impact exhibits a color change
C. Heavy Impact exhibits a different or more intense color change

Dye Filled Microcapsule Synthesis

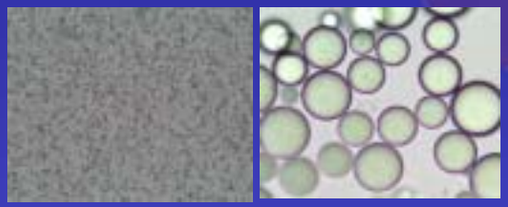

- Homogeneous distribution of microcapsule size / shape
- Microcapsules diameter can be varied between 1-50 μm to attain the desired breaking strength

Advantages of Impact Indicator Paints

- **Quick, simple detection**
  - Impact incidents on an area less than 0.5 cm^2 are readily observable by the naked eye at distances exceeding 6 ft away
  - No external mechanical or electronic equipment is necessary
  - Other impact sensors require external auxiliary equipment
- **Inexpensive and lightweight**
  - The incorporation of low amounts (<10%) of additives will not impact the cost, or the performance of aircraft coatings, or add weight
  - Other impact sensor systems require additional expensive equipment, and can add significant weight and cost to the structural components of the aircraft.
- **Easy to apply**
  - The use of small amounts of the microencapsulated additives will ensure that the procedures for application will be similar to those currently used
  - The use of a paint as a host allows simple reapplication after repairs have been made
  - Reattachment and configuration of other sensor systems is very complicated, if not impossible after repair of aircraft.

Impact Testing for Selected Formulations

Visible Dyes versus Fluorescent Dyes

Advantages for the use of fluorescent microcapsules:

- Fluorescent dyes can be tailored such that impact will only be visible under excitation by a UV source i.e. black light
- Fluorescence will provide a more easily observable color change
- Lower concentrations of dye microcapsules are required – minimal impact on properties
- Impact damage can be quantitatively evaluated with the use of a handheld Fluorometer
- The color of the indicator is not important – fluorescence will work with any color to show excellent contrast

Use of Fluorescent Dyes for Quantifying Impact Damage

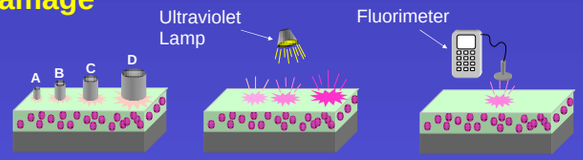

1. Impact incidents of varying energy strike composite – no visible color change is observed
2. UV excitation with a handheld 'black light' will indicate areas where impact incidents above a threshold energy have occurred
3. A handheld off the shelf fluorometer can measure the fluorescent intensity and relate back to quantify calibrated impact energy

Next Steps

- **Fluorescent Dyes** – Use of fluorescent dyes such that impact is only visible under a simple "black light"
- **Quantify impact energy** – Measure fluorescence above a threshold energy, and relative impact energy with intensity
- **Scale up fabrication** – Luna is teamed with a microcapsule manufacturer able to produce multi-ton quantities. We have also teamed with a major coatings manufacturer for prospective commercialization and MIL SPEC qualification
- **Spray coating** – Large components will be coated with conventional painting equipment to evaluate the processibility of our materials. Luna has teamed with an aerospace prime contractor for validation and commercialization.
- **Validate coatings** – meet MIL Specifications for aircraft composite paints

[1] Luna Innovations – Blacksburg, VA
[2] Southwest Research Institute – San Antonio, TX

Contact: Dr. Bryan Koene
540-558-1699
koeneb@lunainnovations.com
www.lunainnovations.com

Spectrum Coupon Testing of ForceTec® Rivetless Nutplate for Aging Military Aircraft

USAF Aircraft Structural Integrity Program
November 29 – December 1, 2005
Memphis TN, USA

Fraser J. McMaster[1], Michael P. Blinn[2], Peter C. McKeighan[1], and Mark L. Thomsen[2]

[1] Southwest Research Institute, San Antonio TX
[2] USAF, Hill AFB, Ogden UT

Introduction

An experimental program of work was undertaken to assess the life improvement gained through utilizing cold expansion (Cx) technology to enhance the resistance of crack nucleation and propagation at fatigue critical wing locations in the T-38 military trainer aircraft. The T-38 program is currently fatigue testing a prototype –33 wing. This wing is designed to double the economic life of the T-38's current –29 wing. However, prior to introducing the –33 wing into service, the USAF intends to manufacture 55 interim –29(I) wings that use the same configuration as the –29 wings with the addition of various design improvements.

The rivetless nutplate, or ForceTec system, utilizes an interference fit to hold the nutplate in place as opposed to the two satellite hole fasteners for the conventional nutplate.

One of the design improvements examined in this testing utilizes a design system called the ForceTec® rivetless nutplate (FtCx™). This system consists of a retainer expanded into a hole, which imparts a beneficial cold worked field around the hole. A nut is then captured in the retainer through which a fastener can then be torqued into place.

Experimental Overview

Evaluation of the influence of cold expansion on spectrum crack growth and total fatigue life, including crack nucleation and propagation, was undertaken. Testing variables and conditions examined included:

- bushed (non-FtCx) and cold expaned (FtCx)
- initial crack size (no crack, 5-, or 25-mils)
- edge margin (e/D) for the FtCx hole (low and nominal)

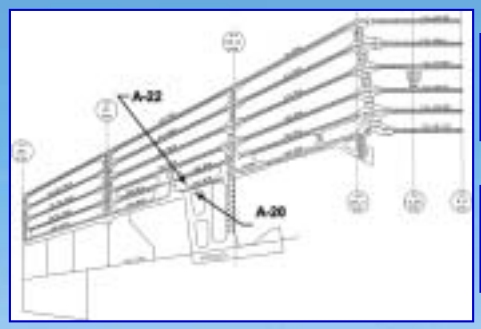

FCL A-20

FCL A-22

Two wing fatigue critical locations (FCLs) were selected for spectrum crack growth testing, with the ForceTec fastening system replacing a conventional nutplate with satellite holes in the –29 wing design. Both FCLs are on the lower wing along the 44% spar, with A-20 on the D-panel at W.S. 73.0 and A-22 at W.S. 92.0.

Both (S-N) fatigue and crack growth testing were performed under spectrum loading conditions, with the stress sequences based on flight recorded data from the Introduction to Fighter Fundamentals (IFF) usage:

- Represents pilot training conducted by the Air Education Training Command
- Randolph and Columbus Air Force Bases
- Sequence represents 1000 hrs of IFF usage and includes 1219 flights

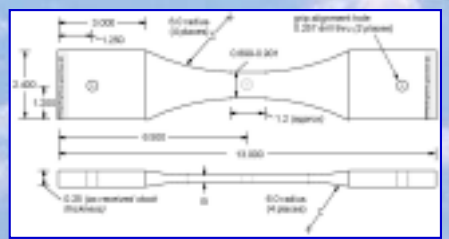

Coupon used to simulate FCLs A-20 and A-22. Experimental setup indicates the cutouts in the fastener head, required to visually monitor crack growth.

Acknowledgements

This test program was conducted under DESP Contract No. F42620-00-D-0037. Gratitude is expressed to Mr. Ramon Castillo (USAF, Hill AFB) for overseeing this contract.

Experimental Results

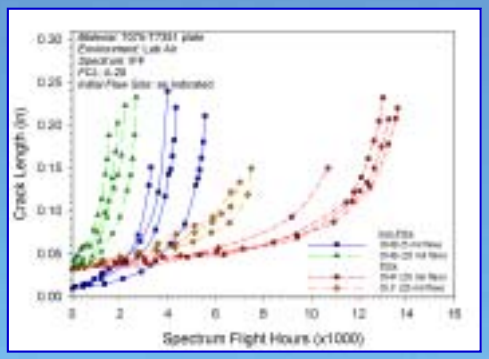

FCL A-20.

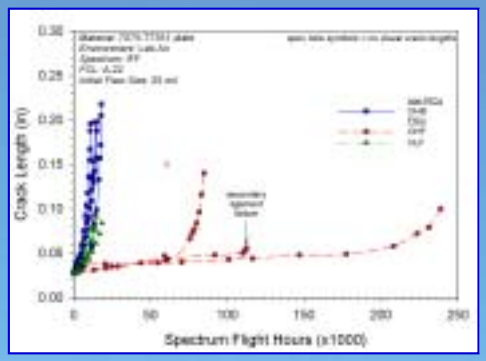

FCL A-22.

Spectrum crack growth test results for FCL A-20 and A-22, comparing the effect of different variables (cold expansion, edge margin, and initial crack size) on the subsequent spectrum crack growth behavior.

FCL	Test Variables	Fatigue Ratio
A-20	Non-FtCx vs. FtCx	5.10
	Low e/D vs. Nominal e/D	1.16
A-22	Non-FtCx vs. FtCx	2.35
	Low e/D vs. Nominal e/D	1.69

Average fatigue life ratios for the non-FtCx and FtCx nutplate coupons indicating life improvement after FtCx processing.

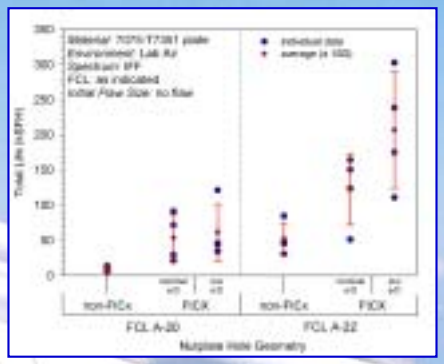

Comparison between the different variables considered in this test program for the non-flawed nutplate coupons for both FCL A-20 and A-22.

Summary

The pertinent experimental results from fatigue (S-N) and SCG testing of FCLs A-20 and A-22 are as follows:

- Average fatigue life for FtCx coupons increased 5.10x (FCL A-20) and 2.35x (FCL A-22)
- Small increase in average fatigue life for the low e/D coupons compared to the nominal e/D coupons (1.16x for A-20 and 1.69x for A-22)
- Fatigue life improvement not found to be statistically significant (student t-test, $\alpha = 0.05$)
- 2x increase in SCG life found for non-FtCx coupons with 0.005 inch precracks compared to 0.025 inch precracks (FCL A-20)
- Increases in SCG life obtained for the FtCx coupons (1.5x low e/D, 3x nominal e/D) compared to the non-FtCx coupon (0.005 inch precrack)
- 3x increase in SCG life found for FtCx coupons compared to non-Cx coupons (FCL A-22). No increase in SCG life for low e/D FtCx coupons compared to non-Cx coupons

Non-FtCx flaw = 0.005 inch

Non-FtCx no flaw

FtCx – nominal e/D flaw = 0.025 inch

FtCx – low e/D flaw = 0.025 inch

SURFACE AND SUBSURFACE EDDY CURRENT INSPECTIONS
Demonstration of Computer Modeling Advantages for Typical Procedures

Evgueni Iordanov Todorov
EWI
1250 Arthur E. Admas Drive
columbus, OH 43221
www.ewi.org

INTRODUCTION

This study addresses the use of computer modeling for procedure development, optimization and validation. Complex and expensive calibration and experimental specimens with artificial and natural flaws are designed, manufactured, and delivered for procedure development. Equipment (probes, instruments, accessories) and personnel have to be scheduled and made available for physical trials. The use of computer modeling and simulation reduces the scope of physical trials, cost and time for NDT technique and procedure development.

MODELING OF SHIELDED PENCIL PROBE OVER STEEL PLATE COVERED WITH COATING

Steel parts coated with highly conductive coatings are difficult for inspection with surface eddy current probes because of coating thickness variation and possibility of cracks propagating under the coatings. The 3D solid model shows typical shielded pencil high-frequency probe (coil with ferrite core) over carbon steel substrate (dark) covered with aluminum coating (greenish).

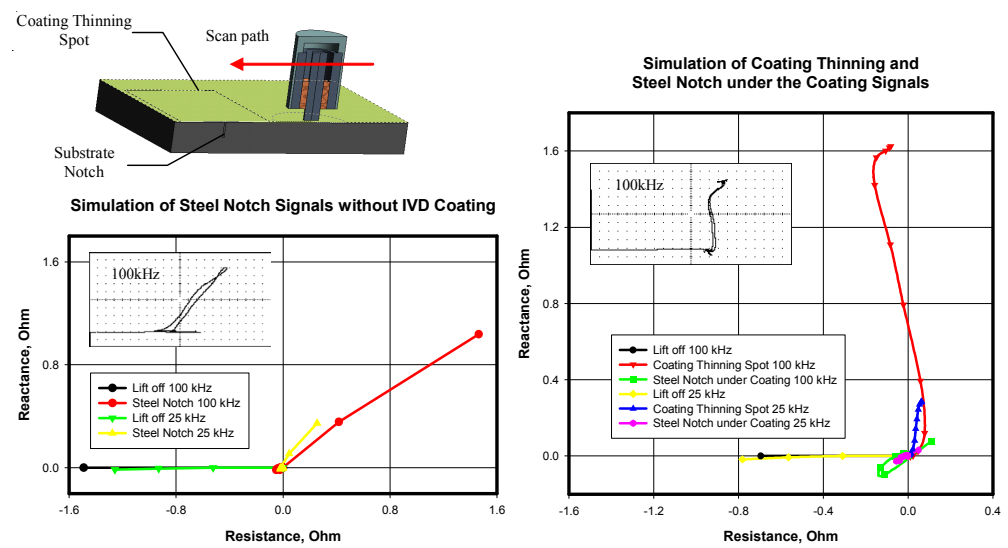

Actual and FEM 3D simulated notch and coating thinning signals for pencil probe over steel substrate without (left) and with (right) aluminum alloy coating.

The combined modeling signal plots show that if the steel notch is covered with the coating, it is practically undetectable. Because an actual crack is tighter than an EDM notch, it will be more difficult to detect the actual crack with the same depth and length as the modeled notch. The results also confirm previous field experience that very small coating thickness variations generate significantly stronger signals than large substrate notches at the frequency range and probe types commonly used for surface inspection.

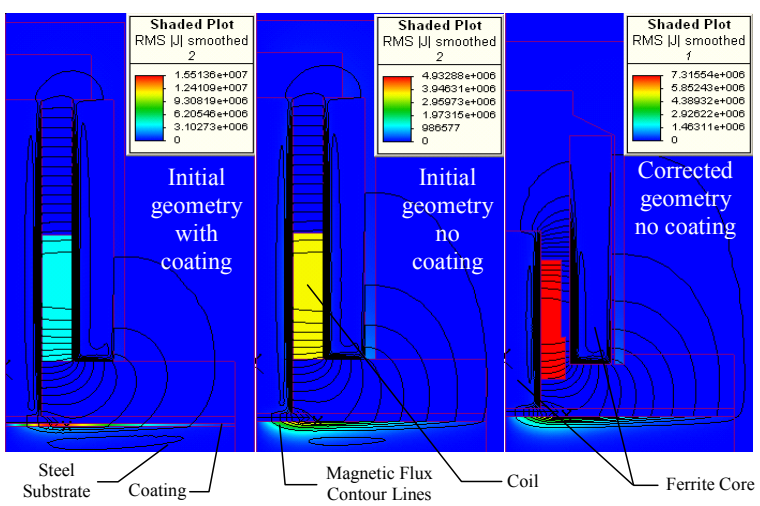

FEM 2D comparison of initial and corrected geometry fields at 100 kHz. Magnetic flux and eddy current density (RMS IJI) distributions.

The color and contour maps with the blue-print and corrected probe geometry explain why the coating thickness variations may generate strong signals at higher frequencies usually used for surface eddy current inspection. The eddy current density is very strong in the coating and the field penetration is insignificant in the substrate. All modeling results indicate that the probe frequency range and design should radically be changed if flaws under the coating are to be reliably detected.

MODELING OF SLIDING PROBE OVER MULTILAYER STRUCTURE

The solid model pictures illustrate the complex probe and specimen geometry, mesh patterns, probe, and notch positions. The transmitter coil follows the receiver coil during scanning. The signal in the receiver coil shown in the plots is result from geometry and property changes in the probe effective area – a 3D area of the space located approximately at the middle between the coils.

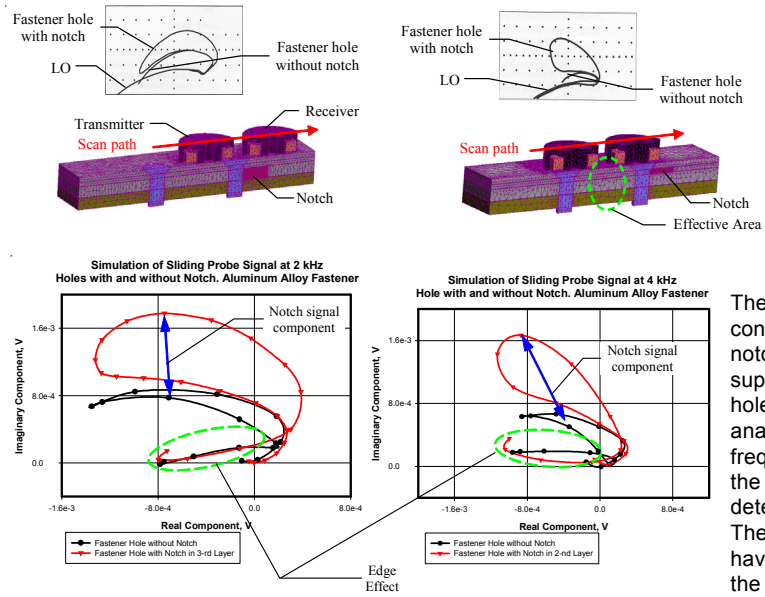

Simulated and actual fastener holes signals with and without notch in the third and second layer for sliding probe over multilayer structure.

The complex shape signal consists of two components: notch signal component superimposed on fastener-hole signal without notch. The analysis indicates that the frequency of 2 kHz is close to the optimal frequency for detection of third-layer cracks. The frequency of 4 kHz may have to be increased so that the signal component from the notch in the second layer becomes perpendicular to the fastener-hole signal without notch.

The notch signal component is almost unaffected by the fastener material and size change. The appearance or shape, though, of the combined signal that will actually be represented on the screen of the eddy current instrument will change depending on the fastener material and size. It means that the field inspection procedure and especially acceptance-rejection criteria has to be adequately designed and carefully worded to account for any possible deviations between the calibration specimen and actual inspected structure. One trend shown in the model results is the decrease of fastener-hole signal when the frequency is increased. This trend is also present in the actual data. Regardless of the shape deviations, the phase and amplitude relations of the fastener-hole signals with and without notches are adequately modeled. The actual signals confirm the adequacy of the models.

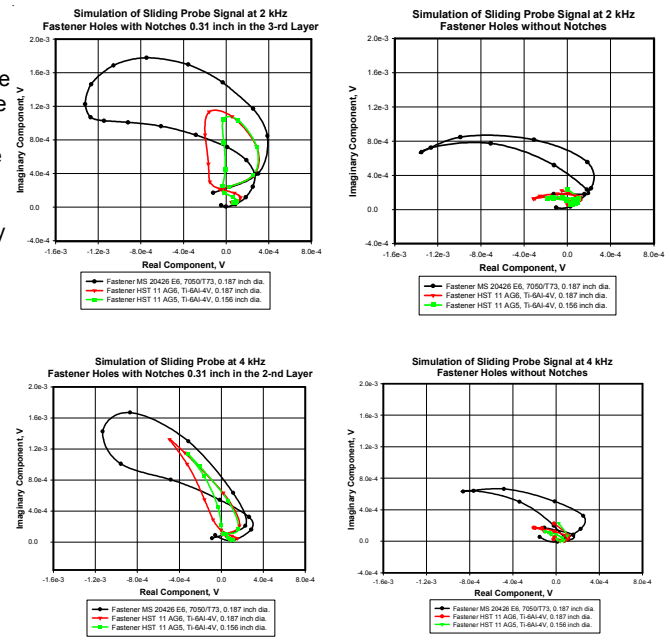

Comparison of signals from fastener holes with fasteners made of various materials and size for sliding probe over multilayer structure. Edge effect signal is removed for clarity.

CONCLUSIONS

The modeling results demonstrate the advantages of computer simulation if implemented into the eddy current technique development optimization, and validation process. The possible benefits are summarized as follows: (1) Significantly reduced time for optimization of procedures used for inspection of complex geometry structures where NDT technique performance is unknown. (2) Significant cost benefits due to elimination and reduction of experimental specimens and mockups. (3) Increased inspection reliability and repeatability. (4) Fast interpretation of field NDE data and reduction of unnecessary repairs. (5) Quick customer support turnaround.

SURFACE AND SUBSURFACE EDDY CURRENT INSPECTIONS. DEMONSTRATION OF COMPUTER MODELING ADVANTAGES FOR TYPICAL PROCEDURES

Evgueni Iordanov Todorov
EWI
1250 Arthur E. Adams Drive
Columbus, Ohio 43221-3585
Phone: (614) 688-5268

ABSTRACT

Significant efforts and resources are dedicated to nondestructive testing (NDT) procedure development. Complex and expensive calibration and experimental specimens with artificial and natural flaws are designed, manufactured, and delivered for this purpose. Equipment (probes, instruments, accessories) and personnel have to be scheduled and made available for physical trials. This paper demonstrates the use of computer modeling and simulation for reducing the scope of physical trials during NDT procedure and inspection development. Two typical inspection cases were modeled: shielded high-frequency probe with complex-shape ferromagnetic core above aluminum alloy-coated carbon steel substrate and sliding low-frequency probe above multilayer aluminum alloy structure with fasteners. The model with pencil-type high-frequency probe investigates the effect of eddy current frequency and coating thickness variations on the detectability of flaws in the steel substrate. The modeling results indicate that substrate cracks might be difficult to detect. The model also shows that small coating thickness variations produce large signals with the probes and frequencies usually used for surface inspections. The model with sliding low-frequency probe illustrates the effect of fastener material and size change on complex (fastener, fastener hole, and flaw) signal shape and appearance. The modeling allows fast and easy interpretation of complex signals obtained with typical sliding probe. The agreement between the modeling data, actual data, physical considerations, and past experience is good. The implementation of advanced modeling tools reduces significantly the cost and time for NDT technique and procedure development. The approach can also be used for fast and reliable customer support turnaround.

INTRODUCTION

Optimization of nondestructive testing (NDT) techniques and methods at the developmental stage and later in-service has always been a key factor for successful technique implementation and performance. Typically, physical specimens and full-scale mockups with embedded natural and artificial flaws are used for optimization and later for validation. The experiments with specimens are complex, expensive, and time consuming when a large number of parameters influence the NDT technique performance.

Currently, computer simulation and modeling are tools that help bridge the gaps in traditional approaches and minimize significantly the developmental costs.

During the past five years, the NDT group at Edison Welding Institute (EWI) has incorporated modeling and simulation tasks in many projects based on ultrasonic

inspection technique. To develop further EWI NDT capabilities, a project work was initiated in the area of eddy current inspection modeling and simulation. Eddy current techniques have been used for many aerospace and power plant inspection applications. Recently, other industries like oil and gas are considering some eddy current techniques for production and service tasks.

To gain proficiency, verify the performance of modeling software, and establish procedures for post-processing of the modeling results, several typical cases were modeled [1, 2]. Two of these typical inspection cases discussed in details further are as follows: shielded high-frequency probe with complex-shape ferrite core above aluminum alloy-coated carbon steel substrate and sliding low-frequency probe with complex-shape ferrite cup-core above multilayer aluminum alloy structure with fasteners. The modeling results were mainly compared to past field experience or well-known eddy current practices and procedures. A limited number of measurements were conducted for qualitative rather than quantitative verification of modeling results. It is realized that thorough experimental model validation is necessary for any practical task. This activity, however, is outside the scope of this initial stage of the modeling project. Deviations between measurements and modeling results were mainly attributed to insufficient data regarding probe design, and probe and inspected material electromagnetic properties.

The eddy current inspections were modeled with two-dimensional (2D) and three-dimensional (3D) analytical modeling (AM) software and 2D and 3D finite-element modeling (FEM) software. The AM package is customized for typical inspections. It is fast but limited to uniform materials, single simple flaw, and simple probe configurations. The FEM package is very flexible. It is designed to model any electromagnetic device or probe with any combination of inspection material anisotropy (multilayer, magnetic and non-magnetic, layer gaps, etc.) and flaw size, location, shape, and orientation.

RESULTS AND DISCUSSION

Modeling of Shielded Pencil Probe over Steel Plate Covered with Coating

An interesting practical problem to investigate is the detection of cracks under surface conductive nonmagnetic or magnetic coatings. The common practical assumption is that if a crack is present in the substrate, it will break through the coating because the substrate and the coating are expected to act as one body in terms of stress-strain distribution. Then, any surface inspection technique capable of detecting the crack in the coating will be considered sufficient for detecting cracks in the substrate. In some cases, however, the coating can be removed, the inspection performed, and later all other substrate inspection have to be carried out through the coating. One possibility is that small cracks can propagate under the coating without breaking it. Another possibility is that the crack in the coating may not have the size and propagation rate of the substrate crack because of a significant difference in substrate and coating mechanical properties. The most recent large-scale comprehensive fatigue study [3] has confirmed the possibility (considered remote in the past) of crack propagation without breaking the cladding or coating. As a consequence, the surface inspection technique might not detect the substrate crack or the crack size in the coating may not be representative of the substrate crack size. Very few studies [4] are available in the open literature to discuss the inspectability of substrate cracks and flaws at this time. It is partly explained with the fact that implanting or growing natural flaws in the substrate and the coating independently or in any combination is very expensive or impractical.

In addition, coated steel parts are often difficult for inspection because of coating thickness variation. It will be shown further that very small variations of coating thickness may produce strong signals that will mask larger substrate crack signals. This is particularly true for cases where surface high-frequency eddy current probes are used for surface inspection of materials coated with highly conductive coatings.

The typical inspection case is steel material covered with aluminum alloy coating. The sacrificial corrosion protection coating is ion vacuum deposited (IVD) over the steel substrate. The 3D solid model in Figure 1a shows typical shielded pencil high-frequency probe (coil with ferrite core) over carbon steel substrate (dark) covered with aluminum coating (greenish).

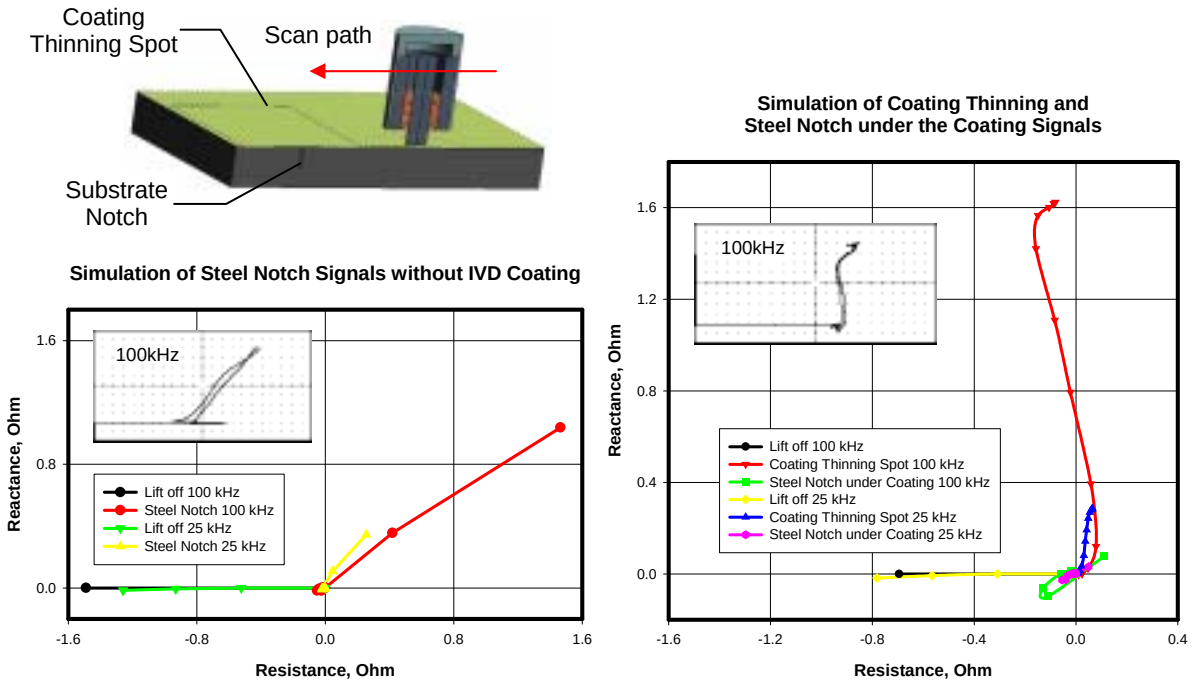

(a) Notch signals without coating

(b) Coating thinning and notch under coating signals

Figure 1: Actual and FEM 3D simulated notch and coating thinning signals for pencil probe over steel substrate without (a) and with (b) aluminum alloy coating.

The steel substrate has the following parameters: 2 mm (0.08 in.) thickness, 40 initial magnetic permeability, and 4 MS/m (6.9% IACS) electrical conductivity. A typical electrical discharge machining (EDM) notch 15.2 × 1 × 0.1 mm (0.6 × 0.04 × 0.004 in.) is built into the substrate. The notch does not propagate through the coating. The coating has a thickness of 0.05 mm (0.002 in.) and conductivity of 18.8 MS/m (32.4% IACS). The coating thickness variation is represented with a spot of 15.2 × 5.8 mm (0.6 × 0.23 in.) where the thickness drops from 0.05 to 0.038 mm (0.002 to 0.0015 in.). The modeling values of coating and substrate conductivity and permeability were chosen in the range that is typical for these materials and grades.

The FEM was used to generate all modeling plots. The AM software cannot model multiple layers and multiple flaws. The steel notch signals shown in Figure 1a for two frequencies are modeled without IVD coating on the specimen. The signal amplitude from the 0.04-in.-deep notch in steel substrate is comparable with the signal amplitude from 0.0005-in. deep and 0.23-in. wide thinning spot in the IVD coating shown in Figure 1b. Actual impedance plane signals are shown in Figures 1a and 1b in the left-hand upper corner of each modeling plot. The actual signals for the steel substrate without IVD coating were obtained with the modeled probe and typical off-the-shelf calibration specimen made of 4340 steel. A commercial grade aluminum alloy foil with step thickness change was applied over the 4340 steel specimen to generate actual signals representing the IVD coating thinning. There are differences between the actual and modeled signals. They are caused primarily by the lack of data regarding magnetic permeability, electrical conductivity and exact dimensions of materials used for generation of actual signals. Another reason is the insufficient data concerning probe design and probe material electromagnetic properties.

The combined signal plots shown in Figure 1b illustrate that if the steel notch is covered with the coating, it is practically undetectable. Because an actual crack is tighter than an EDM notch, it will be more difficult to detect the actual crack with the same depth and length as the modeled notch. The results in Figure 1b also confirm previous field experience that very small coating thickness variations generate significantly stronger signals than large substrate notches at the frequency range and probe types commonly used for surface inspection. The ratio of coating thinning signal amplitude to the notch signal amplitude decreases from approximately 12 to 4 as the frequency decreases. Despite this triple decrease of the ratio, even the frequency of 25 kHz is not sufficiently low to produce notch signal larger than the coating thinning signal.

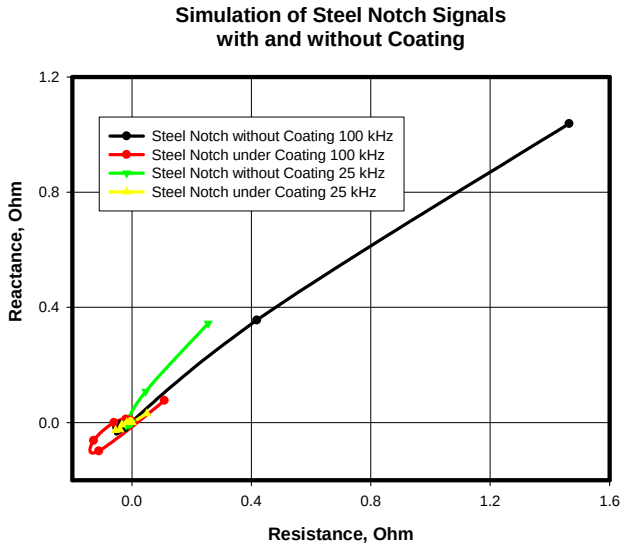

Figure 2: Comparison of simulated notch signals for pencil probe over steel substrate with and without aluminum-alloy coating. The notch does not break through the coating when the coating is present.

For comparison, the notch signals at two frequencies with and without coating are shown in Figure 2. The ratio of notch signal amplitude without coating to the notch signal amplitude with coating is approximately 7 and 13 (17 and 22 dB) at frequencies 25 and

100 kHz, respectively. The shape of notch signal also changes significantly if the coating is present as shown in Figure 2.

Further, the FEM software offers unmatched capabilities in terms of studying the process physics. The 2D models in Figure 3 illustrate the magnetic flux and eddy current density distribution for two probe geometries with and without coating on the steel substrate. Figures 3a and 3b illustrate the filed distribution with the blue-print probe geometry and Figure 3c shows the distribution with corrected probe geometry. The color and contour maps in Figures 3a and 3b explain why the coating thickness variations may generate strong signals at higher frequencies usually used for surface eddy current inspection. The eddy current density is very strong in the coating and the field penetration is insignificant in the substrate.

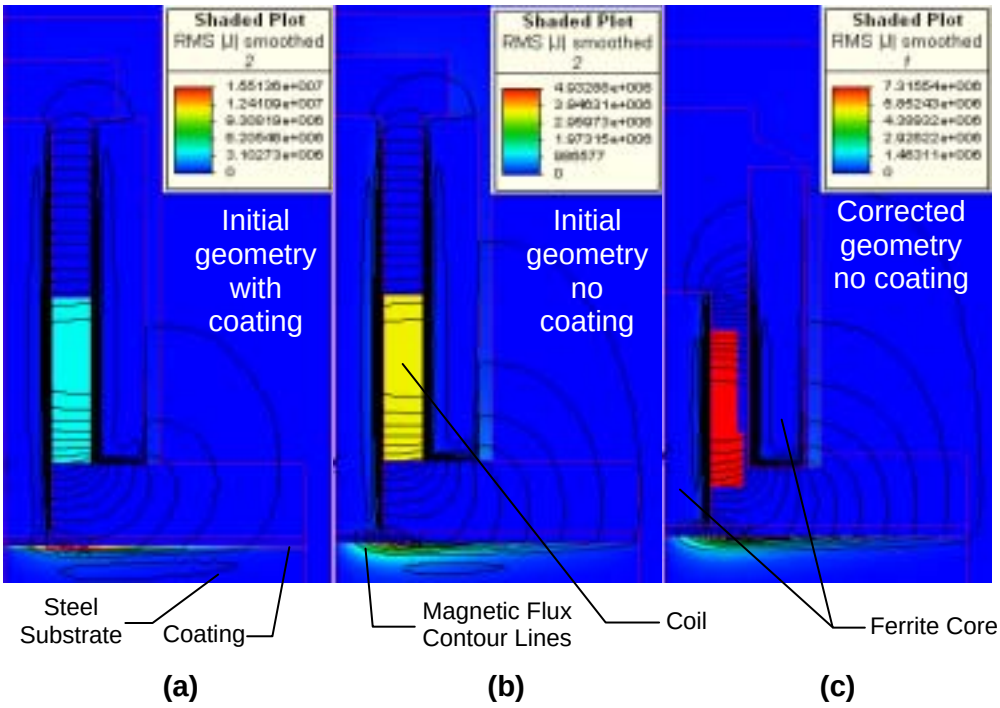

Figure 3: FEM 2D comparison of initial and corrected geometry fields at 100 kHz. Magnetic flux and eddy current density (RMS IJI) distributions.

The reason to investigate the probe design was large discrepancy for probe inductance in air between measured and modeled blue-print values. The 2D and 3D modeling results consistently produced 184 µH, whereas the measured inductance in air was 116 µH. An X-ray radiography allowed correction of geometry as shown in Figure 3c. The modeled 2D and 3D inductance in air with the corrected geometry was 112 µH – a difference of only 3% with the measured value.

In summary, all modeling results indicate that the probe frequency range and design should radically be changed if flaws under the coating are to be reliably detected.

Modeling of Sliding Probe over Multilayer Structure

The low-frequency sliding probe consists of two usually identical coils with or without ferrite core. One of the coils is transmitter the other is receiver. Many publications [5, 6, 7, 8, and 9] discuss practical applications of this type of probes for subsurface corrosion and crack detection. The sliding probe models, however, are not frequent research subject. One of the studies in the past [10] reported modeling results for a sliding probe without ferrite filed concentrators over a single layer and simple flaw shape. The physical interaction between transmitter and receiver coil, and the inspected structure is related to the so-called remote field eddy current (RFEC) phenomenon [8]. The RFEC inspection technique was studied extensively [11 and 12] for tube inspection in the oil, gas, and energy industries. To the author's best knowledge, sliding probe models that account for all geometrical features in the inspected structure and probe configuration are not available in the literature.

The geometrical complexity can only be handled with the FEM software. A sliding probe with complex-shape ferrite cup-core is positioned on a four-layer calibration specimen with aluminum and titanium alloy fasteners, and 7.9-mm (0.31-in.) long EDM notches starting from the fastener holes in the second and third layer as shown in Figure 4. The specimen is made of 2024/T3 and 7075/T6 aluminum alloy sheets with thickness as follows: first layer - 1.5 mm (0.058 in.), second – 1.3 mm (0.050 in.), third – 3.2 mm (0.125 in.), and fourth – 3.3 mm (0.13 in.). The probe is scanned (slid) as shown in Figure 4 along the scan path.

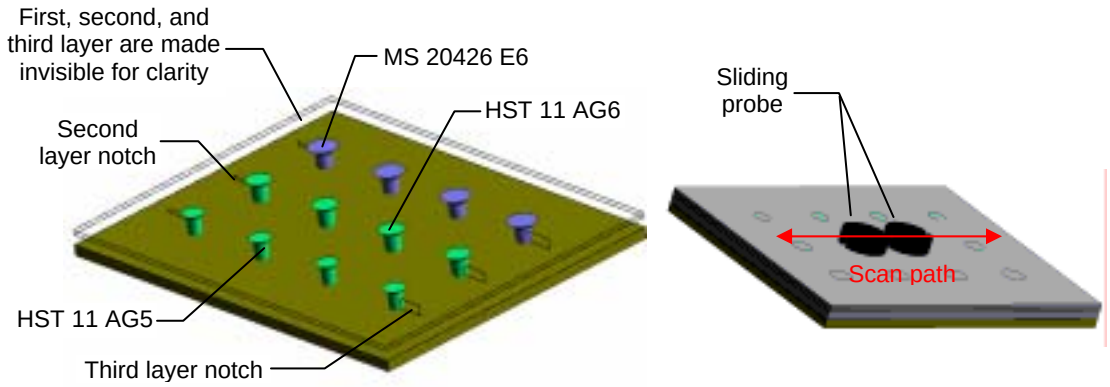

Figure 4: View of multilayer specimen with notches and three types of fasteners. Scanning path of sliding probe over the specimen.

The solid model pictures in Figure 5 illustrate the complex probe and specimen geometry, mesh patterns, probe, and notch positions. The transmitter coil follows the receiver coil during scanning as shown in Figure 5a. The signal in the receiver coil shown in the plots is mainly result from geometry and property changes in the probe effective area – a 3D area of the space (specimen in this case) located approximately at the middle between the coils as shown in Figure 5b.

The modeled signals at two frequencies of 2 and 4 kHz for aluminum alloy fasteners are also shown in Figures 5a and 5b, respectively. Actual flaw detector signals from field procedures with this probe and specimen are illustrated at the top of Figure 5. Software

geometry tolerance limitations cause noticeable signal shape deviation between the model and the actual data. The lift off effect (LO) was not modeled for this probe and consequently the modeled plots were not rotated with respect to the LO signal as they would in any field procedure presented at the top of Figure 5. When the receiver coil is partially or completely off the specimen during scanning and the probe effective area approaches the specimen edge, the obtained signal is referred to as “Edge Effect”.

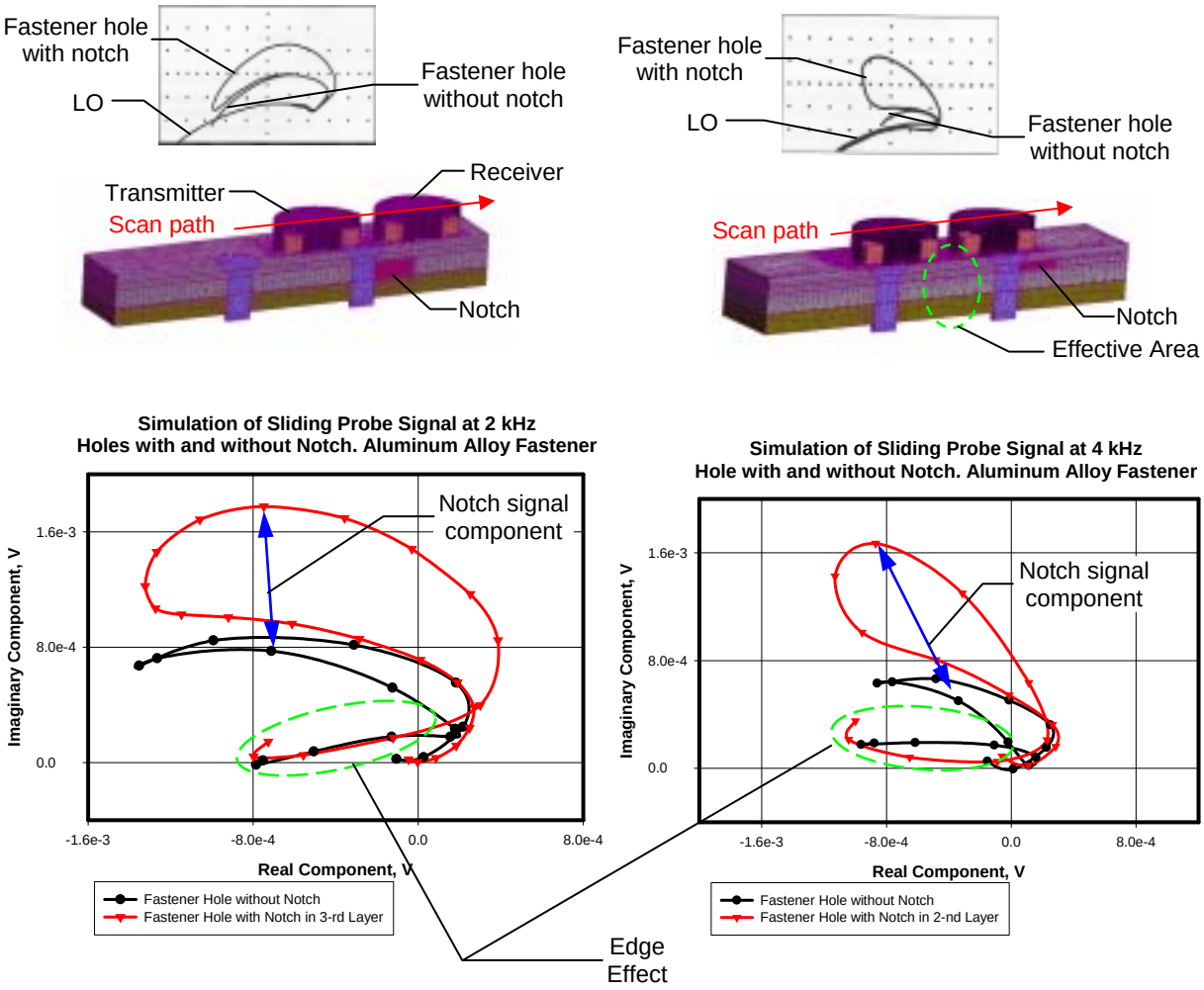

(a) Actual signals, mesh, and simulated signals at 2 kHz

(b) Actual signals, mesh, and simulated signals at 4 kHz

Data for the probe model is courtesy of GE Inspection Technologies

Figure 5: Simulated and actual fastener holes signals with and without notch in the third and second layer for sliding probe over multilayer structure.

As mentioned earlier, the modeling and simulation allows detailed signal analysis to be conducted in a more consistent and systematic manner. As presented in the modeling plots in Figure 5, the complex shape signal consists of two components: notch signal component superimposed on fastener-hole signal without notch. The analysis indicates that the frequency of 2 kHz is close to the optimal frequency for detection of third-layer cracks because the notch component is approximately perpendicular to the fastener-

hole signal without notch. The fastener-hole signal without notch (or crack) is the main signal to discriminate against when inspection with sliding probe is carried out. The frequency, however, of 4 kHz may have to be increased so that the signal component from the notch in the second layer becomes perpendicular to the fastener-hole signal without notch.

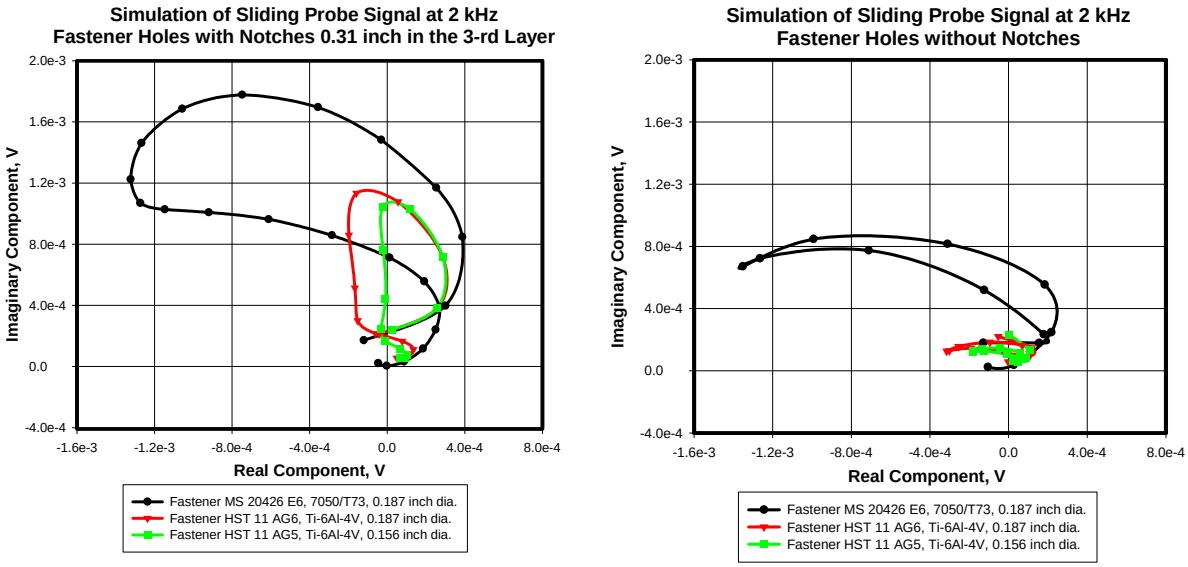

(a) Comparison of signals at 2 kHz with and without notch in the third layer.

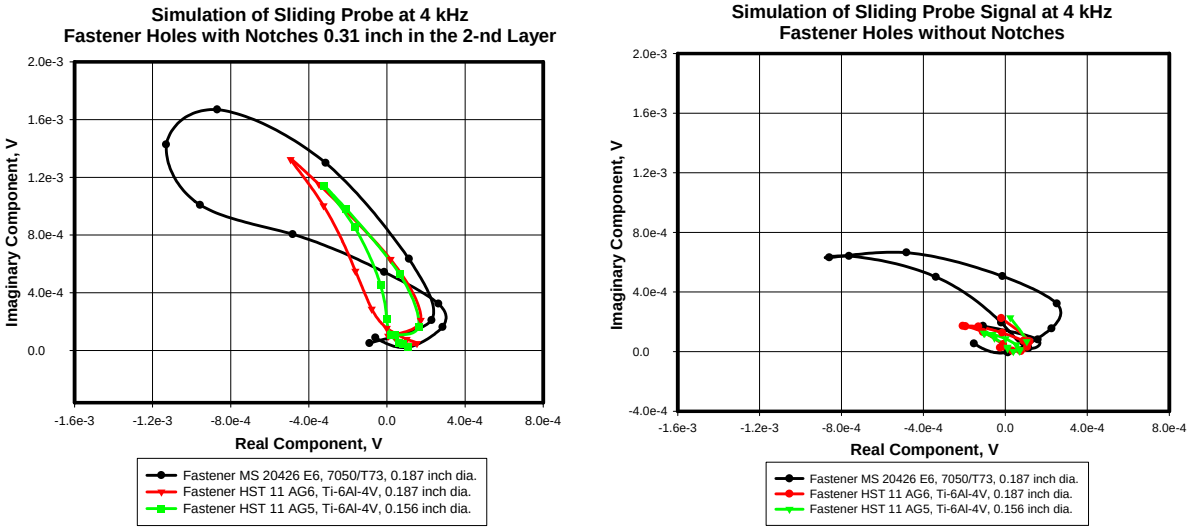

(b) Comparison of signals at 4 kHz with and without notch in the second layer.

Figure 6: Comparison of signals from fastener holes with fasteners made of various materials and size for sliding probe over multilayer structure. Edge effect signal is removed for clarity.

Figures 6a and 6b illustrate the effect of changed fastener material and size on the shape and size of fastener-hole signals with and without notches in the third and second layer respectively. As expected, the notch signal component is almost unaffected by the fastener material and size change. The appearance or shape, though, of the combined signal that will actually be represented on the screen of the eddy current instrument will change depending on the fastener material and size. In practical terms, it means that the field inspection procedure and especially acceptance-rejection criteria has to be adequately designed and carefully worded to account for any possible deviations between the calibration specimen and actual inspected structure.

One trend shown in the model results is the decrease of fastener-hole signal when the frequency is increased. This trend is also present in the actual data in Figure 6.

Regardless of the shape deviations, the phase and amplitude relations of the fastener-hole signals with and without notches are adequately modeled. The actual signals on Figure 5 and other sources [5, 6, and 7] confirm the adequacy of the models. The modeling results show how powerful and flexible the FEM can be for such complex inspection problems.

CONCLUSIONS

Two models of typical complex probes and geometries were developed. The library of typical surface and subsurface probes and specimens provides flexibility and speed when practical tasks are considered.

The modeling results clearly demonstrate the advantages of this approach if implemented into the eddy current technique development optimization, and validation process. The following is a short list of possible benefits and advantages:

- Significantly reduced time for optimization of procedures used for inspection of complex geometry structures where NDT technique performance is unknown.
- Significant cost benefits due to elimination and reduction of experimental specimens and mockups needed for technique and procedure validation.
- Increased inspection reliability and repeatability.
- Fast interpretation of field NDE data and reduction of unnecessary repairs.
- Quick customer support turnaround.

The experience gained so far and developed library of models will further be used to optimize probe design and performance in detection of surface and subsurface flaws and discontinuities, and measurement of inspection area properties for practical inspection tasks.

ACNOWLEDGMENTS

This work was performed under contract with the State of Ohio with financial support from the Ohio Department of Development. The content reflects the views of EWI and does not necessarily reflect the views of the State of Ohio, Department of Development.

The author would also like to acknowledge the cooperation of Bombardier Aerospace Montreal and Toronto divisions in Canada, GE Inspections, Hocking division in U.S., and Olympus NDT, NDT Engineering division in U.S.

REFERENCES

1. Todorov, E. I., “Improvement of Eddy Current Procedure and Inspection Development through Computer Modeling,” *The 48th Annual Air Transport Association of America Non-Destructive Testing Forum 2005*, Orlando, Florida, September 19-22, 2005.

2. Todorov, E. I., “Modeling of Typical Eddy Current Probes and Techniques for Surface and Subsurface Inspections,” *ASNT Fall Conference & Quality Testing Show 2005. Paper summaries*, Columbus, Ohio, pp. 15-22, October 17-21, 2005.

3. Piotrowski, D., “NDT and Damage Characterization of a Retired Passenger Aircraft,” *ASNT Fall Conference & Quality Testing Show 2005*, Columbus, Ohio, October 17-21, 2005.

4. Tracy, N., Davis, S., and Brausch, J., “Nondestructive Inspection (NDI) through High-Velocity Oxygen Fuel (HVOF) Thermal Spray Coatings”, Order 0001: Nondestructive Evaluation Exploratory Development for Air Force Systems, Interim Report for 01 Aug 2001 – 30 May 2002, AFRL-ML-WP-TR-2003-4170, May 2002, pp. 30.

5. Hagemaier, D. J., “Application of Eddy Current Impedance Plane Testing,” *Materials Evaluation*, Vol. 42, pp. 1035-1040, July 1984.

6. Hagemaier, D. J., Bates, B., and Steinberg, A., “On-Aircraft Eddy Current Subsurface Crack Inspection,” *Materials Evaluation*, Vol. 46, pp. 518-522, March 1988.

7. Hagemaier, D. J., “Eddy Current Detection of Subsurface Cracks,” *Materials Evaluation*, Vol. 48, pp. 1074-1082, September 1990.

8. Sun, Y. S., Quang, T., and Udpa, S., “Multi-Layer Aircraft Structure Inspection Using Super-Sensitive Remote-Field Eddy-Current Testing,” *Review of Progress in Quantitative Nondestructive Evaluation*, Vol. 20, pp. 1906-1913, July 2000.

9. Sun, Y. S., Quang, T., and Udpa, S., “Remote Field Eddy Current Testing: One of the Potential Solutions for Detecting Deeply Embedded Discontinuities in Thick and Multilayer Metallic Structures,” *Materials Evaluation*, Vol. 59, pp. 632-637, May 2001.

10. Obrutsky, L. S., Sullivan, S. P., and Cecco, V. S., “Transmit-Receive Eddy Current Probes for Crack Detection,” *CSNDT Journal*, pp. 6-14, September/October 1996.

11. Schmidt, T. R., “The Remote Field Eddy Current Inspection Technique,” *Materials Evaluation*, Vol. 42, pp. 225-230, February 1984.

12. Atherton, D. L., Szpunar, B., and Sullivan, S., “The Application of Finite-Element Calculations to the Remote-Field Inspection Technique,” *Materials Evaluation*, Vol. 45, pp. 1083-1086, September 1987.

X-ray Diffraction Technology: The Current State-of-the-Art for Measuring Residual Stress in Aerospace Structures

J. Pineault, M. Brauss, M. Belassel, R. Drake

Proto Manufacturing Incorporated, 1980 East Michigan Avenue, Ypsilanti, MI, 48198, Telephone: Toll Free (800) 965-5578 or (313) 965-2900 Facsimile: (734) 485-6310 Email: proto@protoxrd.com Website: www.protoxrd.com

INTRODUCTION

Quantitative residual stress characterization of actual aerospace structures and materials is critical to the understanding of structural behavior. Residual stresses are important in the prediction of fatigue life, in assessing the potential for stress corrosion cracking (SCC), in designing repairs and other stress-related issues. It has been common practice in the past to assume certain levels of residual stress. However, because of important advances in the state-of-the-art of x-ray diffraction (XRD) and residual stress (RS) measurement technologies this is no longer necessary. More importantly, robust XRD systems and appropriate components are currently available that enable the quantification of RS in aerospace materials and structures in situ, i.e. in the assembled state.

X-ray Diffraction Residual Stress Measurement

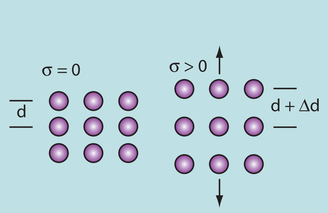

Changes in stress cause changes in atomic lattice spacing "d" and an angular shift of the diffraction peak.

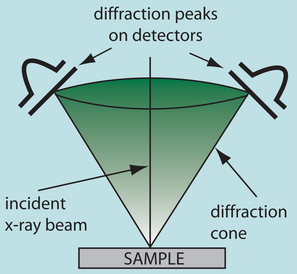

ACCESSING MEASUREMENT LOCATIONS OF INTEREST FOR RESIDUAL STRESS MEASUREMENTS

The challenges put forth by aerospace engineers, OEMs, users and maintainers have led to significant developments and numerous advancements in XRD RS measurement technologies. These challenges are best reflected by such equipment characteristics as "smaller, faster, lighter, more accurate, more reliable, more rugged and more portable." These characteristics have been translated into current technology that exhibits greatly improved accessibility to increasingly tighter and more confined locations in aerospace structures. Technological improvements have been applied where appropriate but more revolutionary concepts have also been implemented to achieve the required levels of miniaturization.

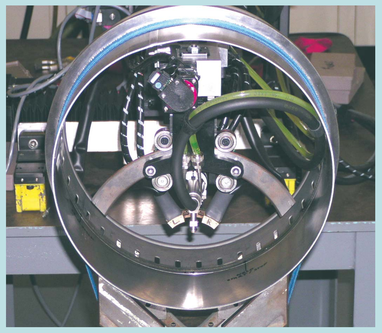

MGR40P goniometer measuring triaxial residual stresses inside a 200 mm diameter bore.

MG40P goniometer measuring residual stresses on an installed aircraft frame.

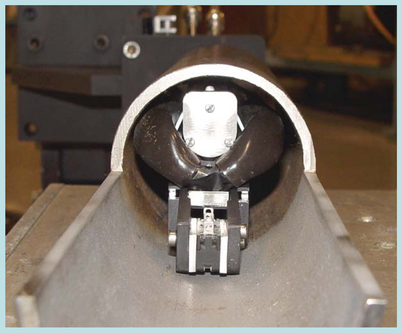

MG15P goniometer measuring residual stress inside a 50 mm bore.

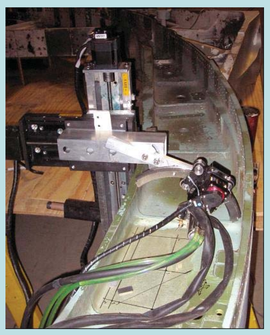

MGR40P goniometer measuring residual stress on an uninstalled aircraft frame.

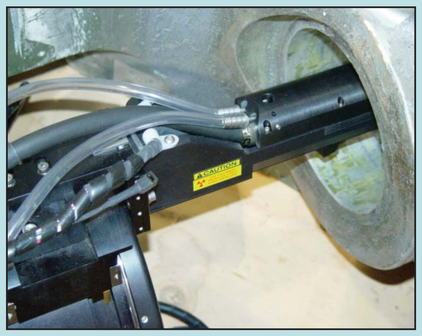

MG30P goniometer measuring residual hoop stresses inside a trunion.

NOVEL GONIOMETER DESIGN

The goniometer in an XRD system, typically contains both the x-ray tube and the x-ray detectors. Historically, goniometers have been quite large and bulky in size. However, significant advances have been made to reduce the overall size of this package and thus enable the device to gain access to the more complicated geometries found in aerospace structural components.

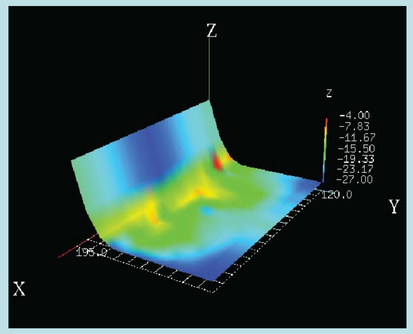

Residual stress map of a web to flange transition on a 7075 Al aircraft frame.

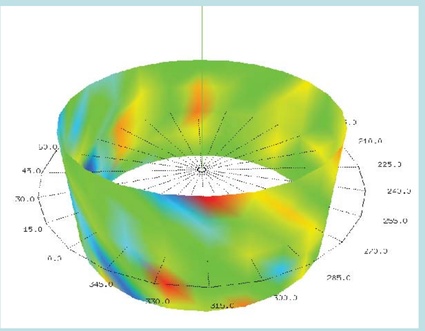

Cylindrical residual stress map inside a main landing gear frame trunion.

RESIDUAL STRESS MAPPING

Due to the increasing speeds in data collection residual stress mapping of areas on a component are now routinely done. Residual stress maps can be generated on flat, curved, cylindrical and spherical geometries using automated X, Y, Z axis translation stages and automated rotation stages.

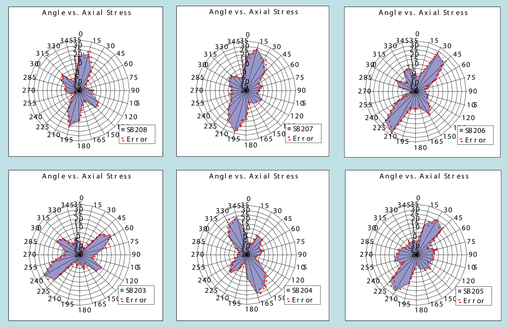

Residual stress maps of SCC dog bone coupons, using automated cylindrical mapping.

SMALLER X-RAY TUBES

Traditionally, x-ray tubes for residual stress measurements have been 30 mm or 60 mm in diameter. Recent advances in x-ray tube technology have enable the creation of 20 mm and 16 mm x-ray tubes. These smaller tubes allow the creation of smaller goniometers and thus access to locations with limited access.

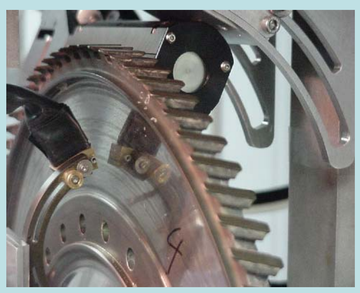

MGBH40L goniometer measuring hoop stress inside a bolt hole.

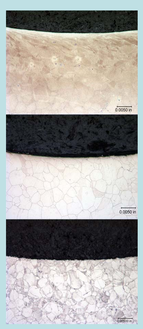

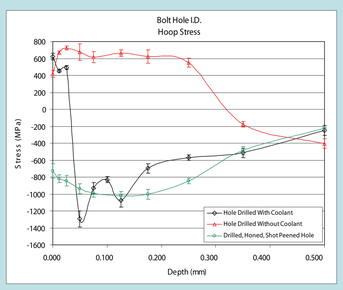

Residual stress vs. depth on bolt holes with different machining parameters. (Used to identify abusive machining)

BOLT HOLE MEASUREMENT

RS measurement on intact components with small diameter bores such as bolt holes are now possible.

ADVANCED DATA ANALYSIS

Residual stress maps can be manipulated graphically and mathematically to enable quantitative before and after measurements. Sound engineering decisions can be made based on real residual stress data.

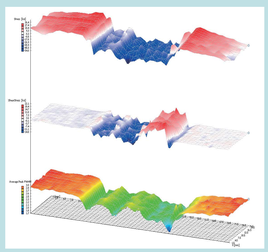

Multi-map with residual stress, shear stress and FWHM maps superimposed or "stacked".

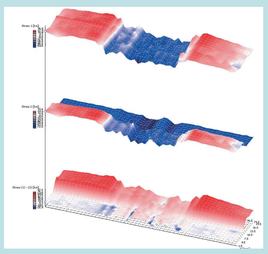

Residual stress multi-map with a third "difference" map plotted by applying map algebra to the first two maps.